NUREG/CR-4149
BNL-NUREG-51857

Ultimate Pressure Capacity of Reinforced and Prestressed Concrete Containments

Prepared by S. Sharma, Y. K. Wang, M. Reich

Brookhaven National Laboratory

Prepared for
U.S. Nuclear Regulatory Commission

NUREG/CR-4149
BNL-NUREG-51857

Ultimate Pressure Capacity of Reinforced and Prestressed Concrete Containments

Manuscript Completed: January 1985
Date Published: May 1985

Prepared by
S. Sharma, Y. K. Wang, M. Reich

Brookhaven National Laboratory
Upton, NY 11973

Prepared for
Division of Engineering
Office of Nuclear Reactor Regulation
U.S. Nuclear Regulatory Commission
Washington, D.C. 20555
NRC FIN A3723

ABSTRACT

This report presents the results of an in-depth evaluation of current modeling techniques and analysis procedures for determining ultimate pressure capacity of reinforced and prestressed concrete containments. The material models used for describing the nonlinear material behavior of concrete and steel are reviewed in detail. Special attention is focused on post-cracking behavior of concrete which controls one of the containment failure modes, i.e., the shear failure. Various finite element idealizations utilized for containment analysis are reviewed. The effects of major assumptions pertaining to containment geometry, basemat restraint, finite element mesh, rebar locations and orientations, are evaluated. Finally, failure analyses of two selected reinforced and prestressed concrete containments are performed and results are compared with those presented in the literature.

EXECUTIVE SUMMARY

Recent analytical studies for the evaluation of ultimate capacity of reinforced and prestressed concrete containments show significant differences in the predicted failure behavior under accident pressures. Essentially, two different failure mechanisms have been obtained for the same containments, namely, shear failure of the concrete at the cylinder-basemat intersection, and extensive hoop yielding of steel in the central cylindrical section. The predicted ultimate pressures for shear failure of the concrete are usually lower than those corresponding to hoop yielding of steel members.

In order to investigate this nonconformity in the analytical results, an in-depth evaluation of current modeling techniques and analysis procedures for concrete containments is performed in this report. The material models used for describing the nonlinear material behavior of concrete and steel are reviewed in detail. Special attention is focused on post-cracking behavior of concrete which controls one of the containment failure modes, i.e., the shear failure. Various finite element idealizations utilized for containment analysis are reviewed. The effects of major assumptions pertaining to containment geometry, basemat restraint, finite element mesh, rebar locations and orientations, are evaluated. Finally, failure analyses of two selected reinforced and prestressed concrete containments are performed and results are compared with those presented in the literature.

The major conclusions and findings are briefly stated as follows:

(1) The shear failure at the basemat-cylinder intersection and the hoop failure in the middle cylindrical section, are both potential failure modes for concrete containments subjected to accident pressures. The analytical predictions for the latter mode of failure are relatively insensitive to various assumptions and idealizations with respect to both material and geometric models. In fact, this failure mechanism can be estimated within a reasonable range of accuracy even with simple hand calculations.

(2) The shear failure mode, however, cannot be predicted by simple analytical models. This failure mode is highly dependent on accurate modeling of the concrete, especially for post cracking behavior and for high compressive plastic deformation. This failure mechanism also requires refined finite element meshes that can properly describe the deformation field in regions subjected to high bending and shear forces.

(3) Since bending and shear deformations are inter-related, the shear failure at the basemat-cylinder intersection is influenced by the locations of the meridional rebars (and tendons) in this region. Simple models in which the steel members are lumped on the inside and outside faces of the containment wall, overestimate the shear capacity of the containment structures.

(4) With respect to the independent analysis, BNL (Brookhaven National Laboratory) in the present study evaluated the failure of the Indian Point and Zion containments under accident pressures and gravity loadings and determined that both of these would fail due to loss of shear capacity at the basemat-cylinder intersection. The failure pressure for the Indian Point Containment is calculated to be 125 psig, while that of the Zion containment is determined to be 111 psig.

(5) In a previous MIT (Massachusetts Institute of Technology) study for the for the Indian Point containment, hoop stress failure is predicted to occur in the cylindrical section. It is estimated that the rebars in this section would reach their ultimate strength at about 200 psig internal pressure. For the same containment, a LASL (Los Alamos Scientific Laboratory) analysis predicts that shear failure at the basemat-cylinder intersection would occur at 118 psig. Although the values for failure pressure predicted by BNL and LASL for the Indian Point containment are close, the actual stiffness and stress conditions are quite different. LASL results show significant compressive crushing of the concrete in the outer areas of the cylinder-basemat intersection, and a corresponding loss of shear stiffness in the crushed region. BNL

region. BNL results show compressive plastic deformation in this region but no compression crushing or loss of shear stiffness. On the other hand, because of computer code limitations in the LASL analysis, a higher shear stiffness is retained for multiply cracked concrete in the tensile region of the intersection. These two effects (i.e., the crushing and higher shear stiffness of multiply cracked concrete) apparently compensate each other in this particular case.

(6) For the Zion containment, an analysis performed by S&L (Sargent and Lundy Engineers) predicts failure due to hoop steel yielding in the middle cylindrical section at 134 psig. LASL reports two failure pressures, one due to shear failure near the basemat-cylinder intersection at 125 psig, and the second due to hoop steel yielding in the cylinder at 136 psig. LASL analysis results, however, show that numerical instabilities develop at 125 psig because of spurious large deformations and yielding of steel members at the dome apex.

(7) Both S&L and MIT used simplified analytical methods which cannot adequately model the deformations and stresses developing under progressive shear failure. This is the main reason that they predicted failure at higher pressures caused by hoop yielding of steel members in the central cylindrical sections. It is BNL's opinion that shear failure takes place at lower pressures as mentioned above.

TABLE OF CONTENTS

TABLE OF CONTENTS (Cont'd)

LIST OF FIGURES

LIST OF FIGURES(Cont'd)

ACKNOWLEDGEMENTS

This work was supported by the U.S. Nuclear Regulatory Commission under FIN No. A-3723. The advice, support and encouragement during various phases of this work given by Dr. C.P. Tan, Dr. P.T. Kuo, and Mr. George Lear of the Structural and Geotechnical Engineering Branch, Office of Nuclear Reactor Regulation are gratefully acknowledged. The authors want to express their thanks to Ms. Joan Murray, Ms. Elizabeth Gilbert and Ms. Diana Votruba for typing this report, and to Mr. S. Shteynyart for assistance in preparing the figures.

1. INTRODUCTION

Structural integrity of nuclear containments under severe accidental pressures due to hydrogen burn has received considerable attention in recent years. For reinforced and prestressed concrete containments several detailed analysis results have appeared in the literature. A comparison of the results, however, shows that different failure mechanisms and failure pressures have often been predicted for the same containment. Essentially, the structural failure is either due to shear failure of the concrete at the cylinder-basemat intersection, or from extensive hoop yielding of steel in the central cylindrical section. Usually the predicted pressure for shear failure is lower than the pressure calculated for hoop yielding of steel members.

The different answers for the same containments found in the literature can be attributed to basic differences in structural models, especially in the material models for reinforced and prestressed concrete and in the geometric idealizations used in the analyses. In order to correctly predict failure in concrete structures, it is necessary to employ suitable material and geometric models that can capture all significant nonlinear effects and mechanisms that ultimately result in loss of structural integrity.

The purpose of this project was to: (1) review and assess the analysis methods and basic assumptions used in the determination of ultimate capacity of the concrete containments, (2) to perform independent failure analysis for selected containments, and (3) to compare the results with those presented in the literature. The findings of this work are detailed in this report.

2. STRUCTURAL MODELING

The failure behavior of concrete containments is influenced by several interacting complex mechanisms, e.g., tension cracking of concrete under multiaxial stresses, plasticity and crushing under compression, shear transfer across cracked sections, yielding of rebars and loss of prestressing in prestressed structures. Most of these effects are simulated in some manner by

the concrete and steel material models chosen for the structural failure analysis. The different material models used for containment analysis are discussed below.

2.1 Concrete Models

Numerous constitutive models have been proposed in the literature to represent the nonlinear stress-strain behavior of concrete. However, most containment analyses have been performed via the application of two types of material models, namely, the nonlinear elastic model and the elastic-plastic model.

2.1.1 Nonlinear Elastic Model

Nonlinear elasticity based models of various forms have been used to represent the stress-strain behavior of concrete. Generally, two different formulations are employed: i) total stress-strain formulation, and ii) incremental stress-strain hypoelastic formulation. The earlier attempt of total formulation for concrete was made by Kupfer and Gerstle,[1] in which a plane stress equation for an isotropic material was derived with the use of secant moduli in shear and bulk. The following constitutive equation between stress components (σ_y, σ_y, τ_{xy}) and strain components (ε_y, ε_y, ε_{xy}) was proposed

$$\begin{Bmatrix} \sigma_x \\ \sigma_y \\ \tau_{xy} \end{Bmatrix} = \begin{bmatrix} D_{11} & D_{12} & 0 \\ D_{12} & D_{11} & 0 \\ 0 & 0 & G_s \end{bmatrix} \begin{Bmatrix} \varepsilon_x \\ \varepsilon_y \\ \gamma_{xy} \end{Bmatrix} \qquad (2\text{-}1)$$

with

$$D_{11} = 4G_s \cdot \frac{3K_s + G_s}{3K_s + 4G_s} \quad , \quad D_{12} = 2G_s \cdot \frac{3K_s - 2G_s}{3K_s + 4G_s}$$

where G_s = Secant shear modulus

K_s = Secant bulk modulus

The moduli G_s and K_s were assumed to vary with octahedral shear and normal stresses, respectively. A similar total stress-strain model was used by Fardis, et al.[2] for analyzing a reinforced concrete containment. The con-

crete was modeled as a linear elastic orthotropic material with elastic moduli that depended on the sign of normal strains in the orthotropic directions along the radial, hoop and meridional axes. Nonlinearity of the concrete in high compression zone was neglected. The elastic modulus was taken to be 3 ksi for the tension-cracked concrete and 3000 ksi for the concrete in compression.

The incremental stress-strain formulation is particularly useful for nonlinear finite element analysis methods which are usually based on incremental solution procedures. Following the same concept as the total formulation, Gerstle[3] proposed the following incremental relationship

$$d\sigma = 3 K_t \, d\varepsilon_o \qquad (2\text{-}2)$$

$$dS_{ij} = 2 G_t \, de_{ij}$$

where $d\sigma_o$ = Incremental octahedral normal stress

$d\varepsilon_o$ = Incremental octahedral normal strain

dS_{ij} = Incremental stress deviators

de_{ij} = Incremental strain deviators

K_t = Tangent bulk modulus

G_t = Tangent shear modulus

and K_t and G_t are, respectively, functions of octahedral normal and shear stresses.

In order to model stress-induced anisotropy, several incremental formulations [4,5] have been developed in which the components of the constitutive (stress-strain) matrix are expressed as functions of principal stresses or strains. In the approach proposed by Bathe and Ramaswamy[5],

different sets of stress-strain relations are derived depending on whether the material is undergoing loading or unloading. A loading function, f, is defined to characterize loading and unloading stress states of the concrete. Using indicial notation and summation convention f is expressed as

$$f = \bar{s} + 3\alpha\sigma_m \tag{2-3}$$

where α is a constant, $\sigma_m = \sigma_{ii/3}$, $\bar{s} = (s_{ij}s_{ij})^{1/2}$, $s_{ij} = \sigma_{ij} - \delta_{ij}\sigma_m$, and δ_{ij} is the Kronecker delta. The loading and unloading conditions are characterized by $f \geq f_{max}$ and $f < f_{max}$, respectively, where f_{max} is the maximum value of the loading function reached under the entire loading history. When the material undergoes unloading, $f < f_{max}$, it is assumed to be isotropic elastic and the initial Young's modulus is used to form the incremental stress-strain matrix.

Under the loading stress state, the stress-strain matrix is evaluated on the basis of three strain components ε_{pi} along the three principal stress directions. Uniaxial tangent Young's modulus, E_{pi}, is then calculated in each principal direction corresponding to ε_{pi} from the uniaxial stress-strain curve. The material is assumed to be isotropic elastic if the maximum of the three principle stresses, σ_{pi}, is greater than $k\,\sigma_c'$ (defined as tension or low compression stress state) where σ_c' is uniaxial compressive failure stress under multiaxial conditions, and k is a constant typically assumed to be 0.4. The equivalent Young's modulus, E, for the isotropic stress-strain matrix is defined by

$$E = \frac{|\sigma_{p1}|\,E_{p1} + |\sigma_{p2}|E_{p2} + |\sigma_{p3}|\,E_{p3}}{|\sigma_{p1}| + |\sigma_{p2}| + |\sigma_{p3}|} \tag{2-4}$$

and the Poisson's ratio is assumed to be the same as the initial Poisson's ratio.

Under high compression stress state, i.e., when the maximum principal stress is less than $k\sigma_c'$, an orthotropic stress-strain matrix is used with orthotropic directions assumed to be the same as the principal stress directions. The stress-strain matrix corresponding to a two dimensional stress state is given by

$$\begin{Bmatrix} d\sigma_1 \\ d\sigma_2 \\ d\tau_{12} \end{Bmatrix} = \frac{1}{(1+\nu)(1-2\nu)} \begin{bmatrix} (1-\nu)E_{p1} & \nu E_{12} & 0 \\ E_{12} & (1-\nu)E_{p2} & 0 \\ 0 & 0 & \frac{1}{2}(1-2\nu)E_{12} \end{bmatrix} \begin{Bmatrix} d\varepsilon_1 \\ d\varepsilon_2 \\ d\gamma_{12} \end{Bmatrix} \quad (2\text{-}5)$$

where ν is assumed to be a constant Poisson's ratio and E_{12} is given by

$$E_{12} = \frac{|\sigma_{p1}|\, E_1 + |\sigma_{p2}| E_2}{|\sigma_{p1}| + |\sigma_{p2}|} \quad (2\text{-}6)$$

The material model described above is available in the ADINA[6] computer code which has been employed for several containment failure evaluations[7,8]. Although this model as well as other hypoelastic models[3,4] have shown good correlations with some experimental data, there are nevertheless questions regarding their applicability under general stress conditions. These are

i) Interaction and cross effects between deviatoric and hydrostatic behavior of the material cannot be properly taken into account by stress-strain relations based on principal stresses and strains as in Eq. (2-5). These effects are important in describing the material behavior under high stresses.

ii) These models implicitly assume that incremental principal stress and strain directions coincide with the principal stress directions, which is not true for general inelastic state of stresses.

In addition, if the principal stress directions are constantly rotating with the loading, coordinate transformations of the stress-strain matrix from the local to the global coordinate systems must be made accordingly. This can significantly increase the computational efforts in the structural analysis.

2.1.2 Elastic-Plastic Model

An elastic-plastic material model was proposed by Chen and Chen[9] to predict the nonlinear behavior of plain concrete. This elastic-plastic model has been used to analyze several concrete structures[10,11] and it has yielded results that are in good agreement with available experimental data. The model has also been employed previously for the failure evaluations of Grand Gulf[12] and Bellefonte concrete containments[8].

The Chen and Chen model uses two different but similar loading functions, f_c, to describe the yielding of concrete in different stress regions as follows:

For compression-compression stress state defined by $\sqrt{J_2} \leq -I_1\sqrt{3}$ and $I_1 \leq 0$,

$$f_c = \frac{J_2 + (\beta/3)\, I_1}{1 - (\alpha/3)\, I_1} = \tau^2 \qquad (2\text{-}7)$$

For tension-compression or tension-tension stress state defined by $\sqrt{J_2} > -I_1\sqrt{3}$ or $I_1 > 0$,

$$f_c = \frac{J_2 - \frac{1}{6}\, I_1^2 + (\beta/3)\, I_1}{1 - (\alpha/3)\, I_1} = \tau^2 \qquad (2\text{-}8)$$

J_2 and I_1 in Eqs. (2-7) and (2-8) are the second invariant of stress deviator and first invariant of stress components, respectively ($J_2 = \bar{s}_{12}$ and $I_1 = 3\sigma_m$). α and β are material constants and τ is a strain hardening parameter. Initial and subsequent loading surfaces defined by these equations are shown in Fig 1 in biaxial stress plane.

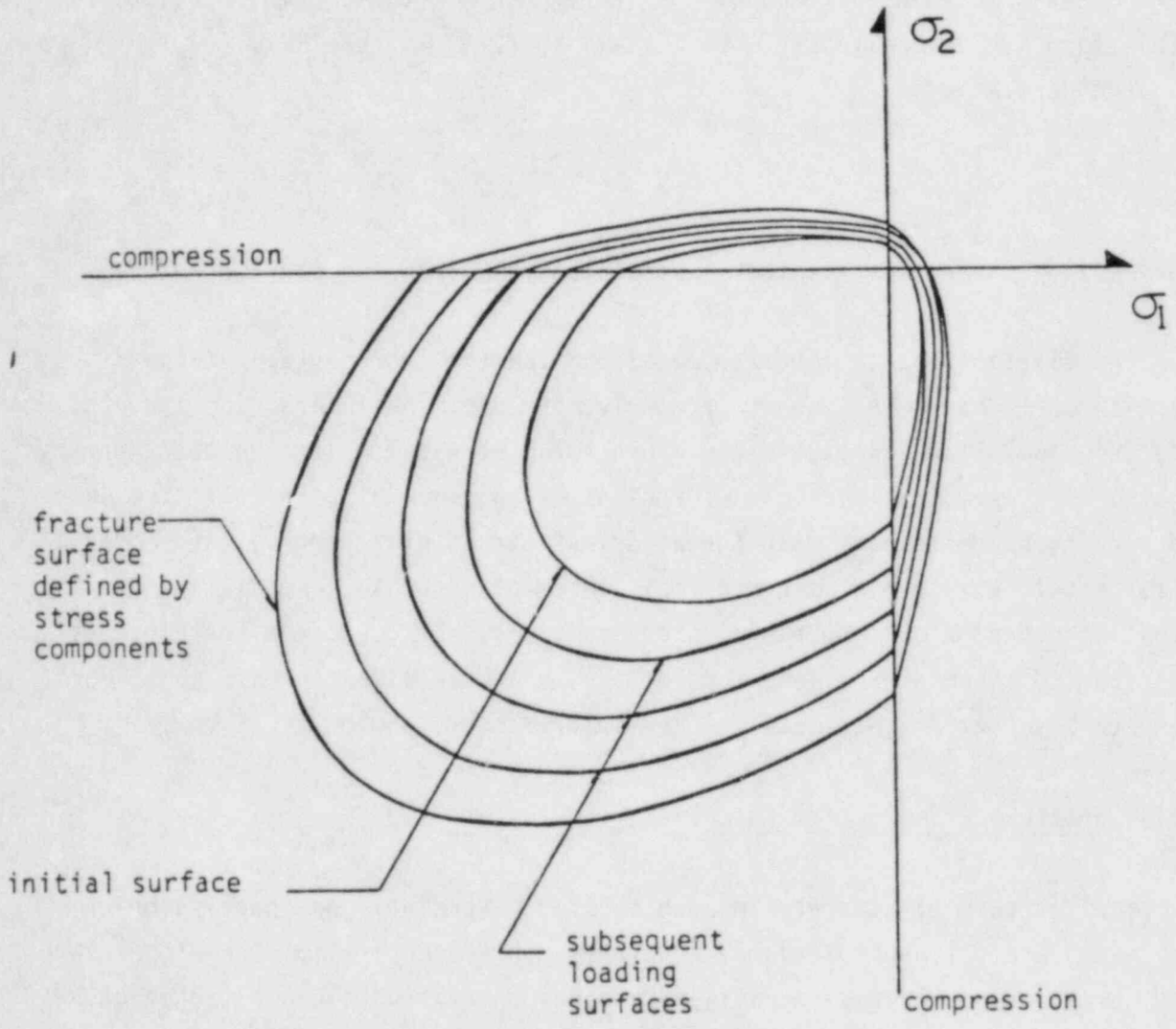

Figure 1. Loading and Fracture Surfaces of Concrete in Biaxial Stress Plane

In the plastic region, incremental plastic strain components, $d\varepsilon^p_{ij}$, are related to f_c by the following associated flow rule of the plasticity theory

$$d\varepsilon^p_{ij} = d\lambda \frac{\partial f_c}{\partial \sigma_{ij}} \tag{2-9}$$

where $d\lambda$ is a material parameter. An incremental stress-strain relation in matrix form can be derived from Eqs. (2-7) to (2-9) as (see Ref. [9] for detailed derivation)

$$\{d\sigma\} = [C_{ep}]_c \{d\varepsilon\} \tag{2-10}$$

where $[C_{ep}]_c$ is an elastic-plastic constitutive matrix for the concrete.

The elastic-plastic concrete model, unlike the incremental nonlinear elastic model, has been shown to properly represent the interaction and cross effects between the deviatoric and hydrostatic stresses. It also does not require the assumption that the directions of incremental principal stresses and strains be coincident with the principal stress directions. This model will, therefore, yield a more realistic material response, especially for situations where high compressive stresses occur. For concrete containments subjected to internal pressure loadings, high compressive stresses have been shown to occur at the basemat-cylinder intersection.

2.1.3 Fracture Criteria for Concrete

The fracture of concrete in both tension (cracking) and compression (crushing) are defined by failure envelopes. Different failure envelopes have been developed by various investigators based on available experimental data on concrete failure under multi-axial stresses. The envelopes used in the ADINA concrete model are described pictorially in Ref. 5 and, as mentioned, they are utilized by many analysts. The Chen and Chen model employs a duel representation of fracture criterion expressed in terms of both stresses and strains. This duel criterion is expressed by the following equations:

Stress criterion

$$f_c = \tau_u^2 \tag{2-11}$$

where f_c is defined in equation (2-7) and τ_u is the fracture strength of the concrete under multiaxial stress.

Strain Criterion

$$g = J_2' + \frac{A_u}{3}\left(\frac{\varepsilon_u}{f'_c}\right) I_1' = \tau_u^2 \left(\frac{\varepsilon_u}{f'_c}\right)^2 \tag{2-12}$$

or

$$\varepsilon_{max} = \varepsilon_t \tag{2-13}$$

where $I_1' = \varepsilon_{ii}$, $J_2' = \varepsilon_{ij}\,\varepsilon_{ij}/2 - \varepsilon_u^2/6$; ε_u and ε_t, respectively, are the fracture strains of concrete under uniaxial compressive and tensile loads, f'_c is the unaxial compressive strength, A_u is a material constant, and ε_{max} is the maximum principal strain. A graphical representation of the strain criterion in the biaxial strain plane is depicted in Figure 2.

When the concrete fractures in a compressive stress state (crushing), its stiffness and stresses in all directions are set to zero. In the case of tensile fracture (cracking), however, only those stiffness and stress terms that are associated with the normal to the cracked plane are reduced to specified minimum values, as discussed below.

2.1.4 Post Cracking Behavior

Due to difficulties with excessive grid redefinition and the other computational complications, the modeling of discrete cracks for conducting the analysis of large-scale reinforced concrete structures is impractical. Consequently, an approximate procedure, in which the cracks are assumed to be distributed over a finite area, has been adopted for most containment failure

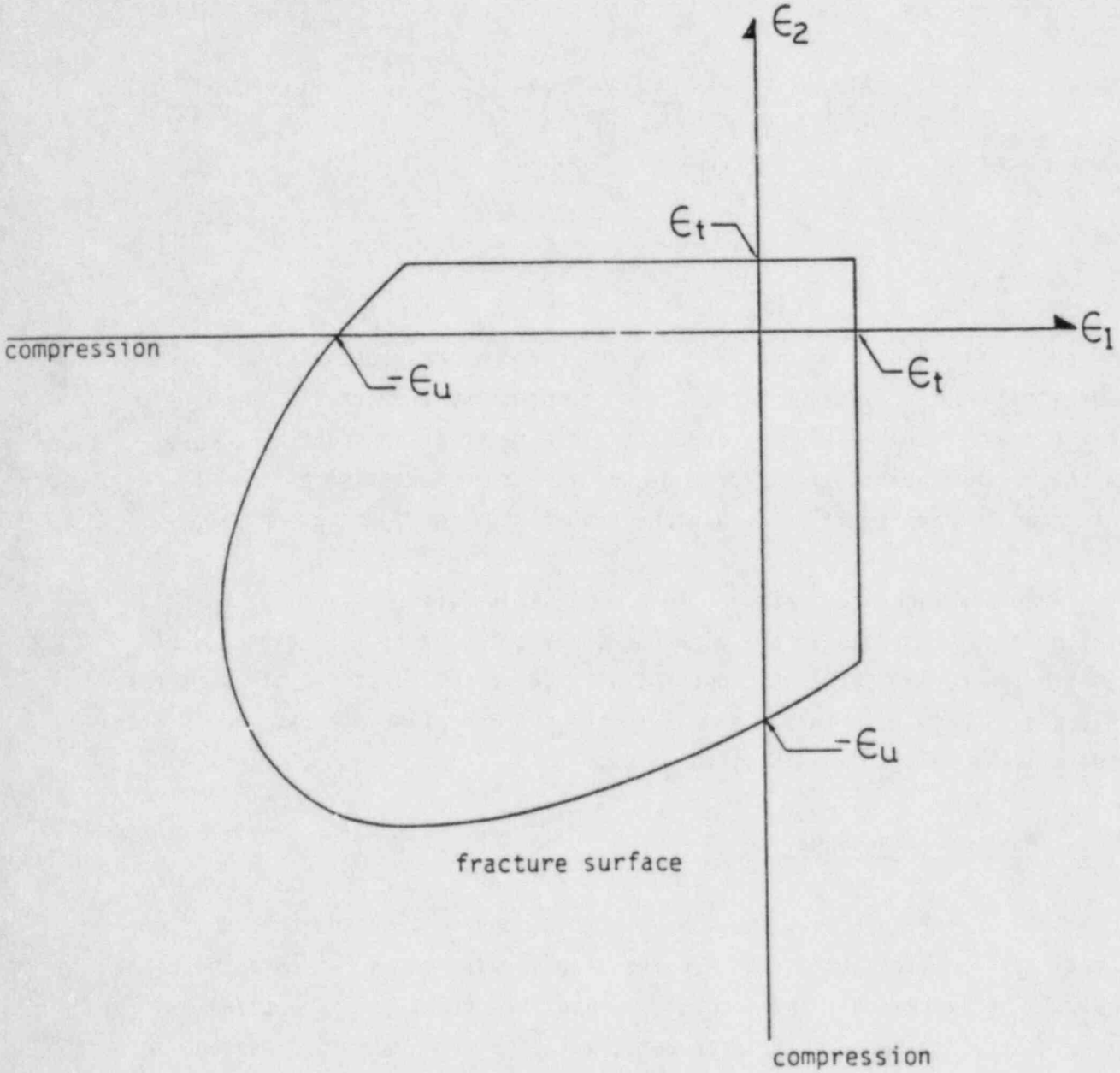

Figure 2. Fracture Surface of Concrete in Biaxial Strain Plane

analyses. The cracking of concrete in this procedure is evaluated at selected points within an element using a specified criterion for the cracking. When cracks occur at a particular point, the material constitutive matrix [D] and the internal stresses at that point are modified in accordance with the specific crack pattern. The cracked concrete is assumed to remain a homogeneous continuum. Thus, rather than representing the physical material separations due to the cracks, the effects of the cracks on structural stiffness and stress redistribution are considered directly. This procedure is illustrated below using a stress-based cracking criterion.

Essentially, the stresses in the concrete (σ_x, σ_y, τ_{xy}) are first transformed to principal stresses (σ_1, σ_2), where σ_1 is greater than σ_2. If the maximum principal stress σ_1 exceeds (algebraically) the tensile strength of concrete, a crack is opened in a plane perpendicular to the first principal direction. The incremental linear or nonlinear constitutive equations for the cracked concrete are then given by

$$\begin{Bmatrix} d\sigma_1 \\ d\sigma_2 \\ d\tau_{12} \end{Bmatrix} = \begin{bmatrix} \alpha D_{11} & \alpha D_{12} & 0 \\ \alpha D_{12} & D_{22} & 0 \\ 0 & 0 & \beta D_{33} \end{bmatrix} \begin{Bmatrix} d\varepsilon_1 \\ d\varepsilon_2 \\ d\gamma_{12} \end{Bmatrix} \qquad (2\text{-}14)$$

where α and β are, respectively, the normal and the shear stiffness retention factors, and D_{11}, D_{12},...D_{33} are the stiffness terms of the uncracked concrete. The normal stiffness retention factor α is usually set to zero or to a very small value. A gradual reduction of α as a function of ε_1 in the cracked concrete has been suggested in some studies in order to model the so-called tension stiffening effect. This effect results from the capability of concrete between the cracks to carry tensile stresses via load transfer through the reinforcement bars. Another reason for decreasing α gradually is to improve the convergence of the numerical algorithm. The shear stiffness reduction factor β is assigned a comparatively higher value (e.g., 0.5) because significant amounts of shear stresses can be transferred across a

crack plane by several shear transfer mechanisms (see Section 2.1.5 for details). In addition to these modifications of the stiffness terms, the principal stress σ_1 is set to zero. This releases the normal stress perpendicular to the crack plane and results in a redistribution of the internal stresses.

The formation of a second crack after the first crack has opened is treated in a similar manner. Starting from a new distribution of stresses ($\sigma_{1=0}$, σ_2, τ_{12}), another set of principal stresses (σ_1', σ_2') is calculated. If the principal stress σ_1' exceeds the tensile strength of concrete, a second crack is opened perpendicular to σ_1'. In general, the first and the second crack planes are not mutually orthogonal. For these two crack planes to be orthogonal, τ_{12} must be zero. The opening of the second crack releases the principal stress, σ_1'.

To adequately model the cracking of concrete under stress reversals which would occur under dynamic loading, the possibility of closing of cracks must also be taken into account. A crack width concept similar to that of Darwin and Pecknold[4] is often used. Using this concept, the crack width for a two-dimensional stress state is determined by

$$C_{wi} = \frac{\sigma_{max}}{E_i} + \sum\left(\Delta\varepsilon_i + \nu\,\Delta\varepsilon_j\right);\ i = 1, 2 \qquad (2\text{-}15)$$

where

C_{wi} = Crack width
σ_{max} = Tensile stress at which the crack is opened
E_i = Tangent elastic modulus prior to crack formation
$\Delta\varepsilon_i$ = Increment of strains
ν = Poisson's ratio
Σ = Summation over all load increments.

Either one of the two cracks may open or close in the subsequent load increments depending upon whether C_{wi}, i=1,2, is positive or negative. The crack is also assumed to be closed if C_{wi} is equal to zero. If both the cracks are open at the same time, the effect of Poisson's ratio in Eq. (2-15) is ignored. The crack widths are then given by

$$C_{wi} = \frac{\sigma_{max}}{E_i} + \sum \Delta\varepsilon_i \qquad (2\text{-}16)$$

When a crack closes, appropriate stiffness terms of the constitutive matrix are restored. The stress perpendicular to the closed crack is monitored in subsequent load increments (or iterations). The crack is opened again if this stress becomes positive and the subsequent crack widths are calculated from Eq. (2-15) or Eq. (2-16) with $\sigma_{max} = 0$.

2.1.5 Shear Transfer

Transfer of shear stresses in cracked concrete influences the redistribution and growth of internal stresses. The shear transfer in tension cracked concrete has been a subject of many studies in recent years. Based on these studies, three important mechanisms for shear transfer across a crack plane are identified as follows:

(i) Interface shear transfer
(ii) Direct tension in normal reinforcement
(iii) Dowel action of main reinforcement

(i) Interface shear transfer - The crack surfaces that are created by tensile cracks in the concrete are usually rough and irregular. This is, in part, due to the zig-zag path that the crack tip has to traverse in order to by-pass the coarse aggregates in concrete. When an external force is applied across a crack (Fig. 3a), the shear displacement between the surfaces is resisted by an interface shear force V_E caused by friction between the surfaces, and by interlocking of the aggregates. The magnitude of this shear force depends not only upon the shear displacement Δ, but also upon the initial crack width C_w and the concrete compressive strength, f_c':

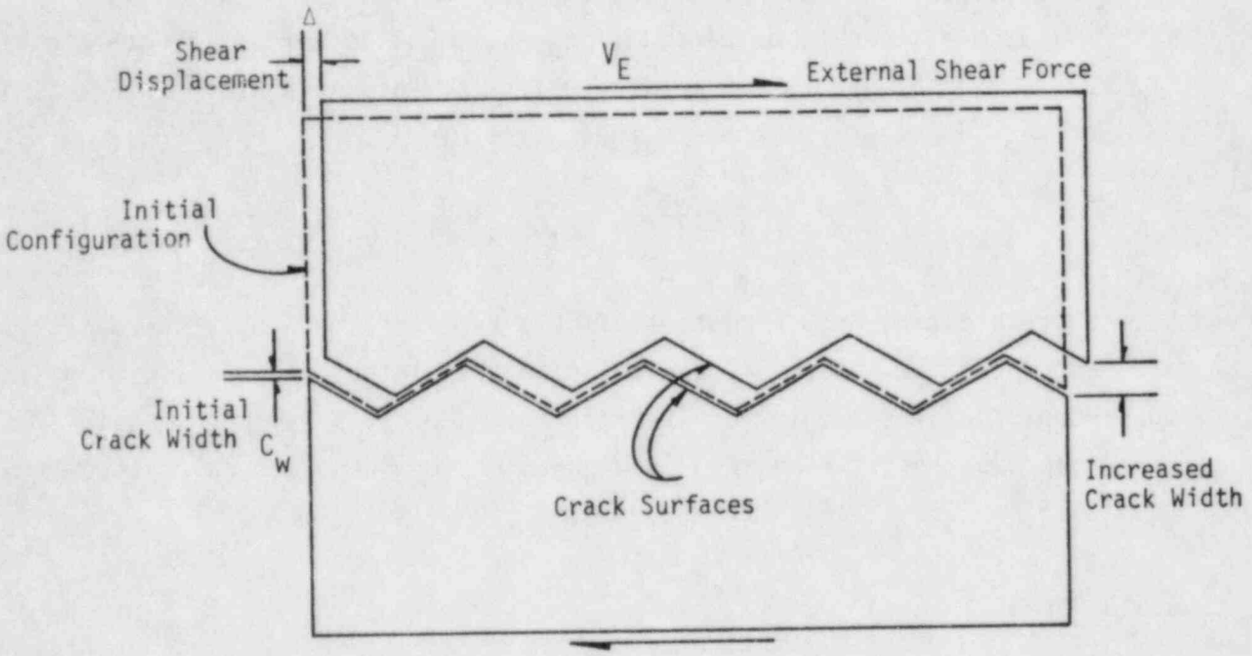

Figure 3a. Interface Shear Transfer Mechanism Across Idealized Crack Surfaces

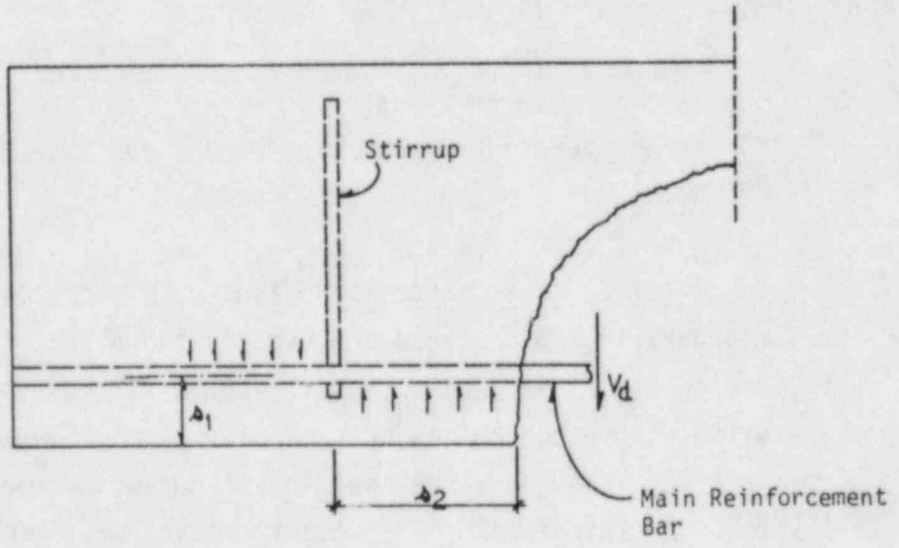

Figure 3b. Shear Transfer by Dowel Action

$$V_E = f(\Delta, C_w, f_c') \qquad (2\text{-}17)$$

Various expressions for the function f in Eq. (2-17) have been proposed based on available experimental data. These expressions show that V_E increases with increasing Δ and f_c'. It decreases, however, with increasing C_w because the frictional contact between the surfaces is reduced at higher values of C_w.

Under cyclic loads, interface shear stresses also depend upon the number and intensity of stress reversals. Experimental results show that cyclic shear stresses gradually increase the crack width and relative slip between the crack surfaces due to the surface degradation resulting from crushing and rounding of the aggregates.

(ii) Direct tension in normal reinforcement - As shown in Fig. 3a, shear displacement between the crack surfaces increases the crack width. The increased crack width causes extension in the reinforcement (usually the web reinforcement) bars placed normal to the crack surfaces. The tension in these bars resists the shear displacement, and thus contributes to the shear stiffness of the cracked concrete. This contribution increases with increasing tension in the bars, but remains constant once the bars have yielded. Moreover, once the bars yield, stiffness contributions from the other two mechanisms (i.e., interface shear transfer and dowel action) would reduce rapidly because of the widening of the crack and the longitudinal splitting that occurs along the main reinforcement.

(iii) Dowel action of main reinforcement - The reinforcement in concrete members usually carries stresses along its axis. When this reinforcement crosses a crack path, it can also carry significant amounts of shear forces by dowel action that involves shear, flexure, and kinking deformations of the reinforcement bars. The maximum shear force V_d in a bar (Fig. 3b) varies with the bar diameter, tensile strength of concrete, cover distance s_1, and stirrup distance s_2 between the crack and the first stirrup supporting the bar. If the cover distance s_1 is too small, V_d can cause splitting of the

concrete along the bar. For large s_1, only localized crushing of the concrete under the bar takes place. In the case of concrete splitting, the cover distance s_2 governs the effectiveness of the dowel action, and consequently the shear force V_d.

Although the effect of the above described three mechanisms on the shear stiffness of cracked concrete may be included in a simple finite element analysis by using special bond-link elements between discrete crack surfaces, this approach is impractical for analyzing large-scale reinforced concrete structures. In the current practice, therefore, the effect of cracking on the shear stiffness of concrete is taken into account by a modification of the constitutive material matrix. Specifically, the shear modulus of the cracked concrete, $\bar{G}$, is expressed as a fraction of the shear modulus of uncracked concrete G (see Eq. 2-14 for a two-dimensional stress state):

$$\bar{G} = \beta G \tag{2-18}$$

In the ADINA[6] computer code, which as mentioned was used by some investigators for containment failure analyses, β is assumed to be constant and equal to 0.5 for all cases including multiple cracks in different directions. This approach obviously ignores the effect of multiple cracks and their widths on the shear stiffness.

Another approach for representing the shear stiffness of cracked concrete was employed by Fardis, et al.[2] for performing a containment failure analysis. Mathematically, the cracked shear stiffness G is given by the equation

$$\bar{G} = \frac{1}{\frac{1}{G} + \frac{1}{l}\,\frac{1.7}{K_n + 1.7\,K_D}} \tag{2-19}$$

where l is the crack spacing, and K_n and K_D are the extensional and dowel stiffnesses of the rebars crossing the crack. A similar expression for two orthogonal cracks was also proposed by Leombruni, et al.[13] for the evaluation of cracked reinforced concrete panels. It should be noted, however, that the use of either Fardis or Leombruni approach for cracked shear stiffness requires apriori knowledge of crack spacings.

Recently Al-Mahaidi and Nilson[14] proposed the following equation based on physical test data and analysis to account for the effect of crack width on the shear retention factor: σ

$$\beta = \frac{C}{\varepsilon_1/\varepsilon_{to}} \qquad (2\text{-}20)$$

where β_1 is the principal tensile strain normal to the crack and ε_{to} is the tensile strain at the initiation of cracking and C is a constant equal to 0.4. This is the expression that has been adopted for the containment failure evaluations performed at BNL.

2.2 Steel Models

Since the reinforcing bars are primarily under tension or compression, uniaxial material models are adequate to represent their stress-strain behavior. For other steel members subjected to multiaxial stresses, e.g., containment liners, material models based on the classical plasticity theory have generally been used. A brief review of both the uniaxial and plasticity models is given below.

2.2.1 Uniaxial Models for Reinforcing Bars

Typical stress-strain curve for a reinforcing bar under monotonic loading is shown in Fig 4. The stress-strain curve has three distinct parts: (1) an initial elastic curve up to the yield point (ε_y, σ_y), (2) a short and almost flat (perfectly plastic) curve between ε_y and ε_{sh}, where ε_{sh} is the strain at which strain hardening is initiated, and (3) a strain hardening curve from ε_{sh} to the ultimate failure point (ε_u, σ_u). The slope of the curve at the failure point is almost zero.

The first two parts of the monotonic stress-strain curve are closely approximated by the following equations:

$$\sigma = E\,\varepsilon \qquad \text{for } \sigma \leq \sigma_y \qquad (2\text{-}21)$$

$$\sigma = \sigma_y \qquad \text{for } \varepsilon_y < \varepsilon \leq \varepsilon_{sh} \qquad (2\text{-}22)$$

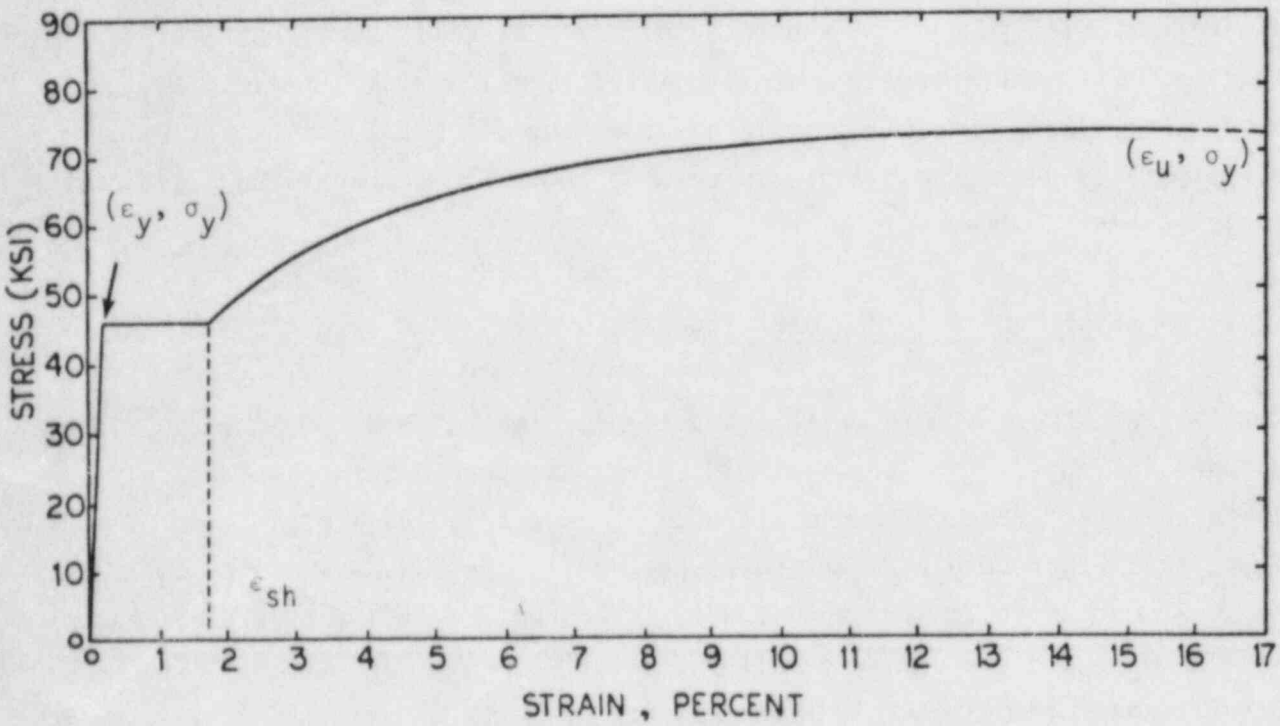

Figure 4. Typical Stress-Strain Curve for Reinforcement Steel Under Monotonic Loading

where E is the elastic modulus of reinforcing steel. The third part of the curve can be represented by expressing σ as a nonlinear function of ε and selected material parameters. Different expressions for the nonlinear function have been proposed by various investigators for their uniaxial models. Thus, for example, the following expression in terms of ε and four material parameters, σ_y, ε_{sh}, ε_u and σ_u, was used by Fardis, et al.[2] in a containment failure evaluation

$$\sigma = \sigma_u - (\sigma_u - \sigma_y)\left(\frac{\varepsilon_u - \varepsilon}{\varepsilon_u - \varepsilon_{sh}}\right)^4 \quad \text{for } \varepsilon_{sh} < \varepsilon \leq \varepsilon_u \tag{2-23}$$

In most other containment analyses, however, the stress-strain curve beyond the yield point has been approximated either by Eq. (2-22) for a perfectly plastic response, or by a straight line connecting the yield and ultimate failure points.

2.2.2 Multiaxial Plasticity Models

The constitutive material models for steel members subjected to multiaxial stresses, such as the liner etc., are generally based on incremental associated von Mises plasticity theory with isotropic or kinematic strain hardening. This theory is based on the following definition of a yield function F:

$$F(s_{ij}, \alpha_{ij}, \sigma_y) = \frac{1}{2}(s_{ij} - \alpha_{ij})(s_{ij} - \alpha_{ij}) - \frac{\sigma_y^2}{3} \tag{2-24}$$

where s_{ij} are deviatoric stresses and α_{ij} are components of a tensor that describes the translation of the yield surface defined by F = 0. Current yield radius of this surface is denoted by σ_y. The yield radius σ_y is a constant equal to uniaxial yield stress for kinematic strain hardening, whereas it is assumed to be a function of plastic work W_p in the case of isotropic strain hardening:

$$\sigma_y = \sigma_y(W_p) \tag{2-25}$$

where W_p is defined as

$$W_p = \int \sigma_{ij} d\varepsilon_{ij}^p \tag{2-26}$$

in which $d\varepsilon_{ij}^p$ are plastic strain increments. There is no translation of the yield surface for isotropic strain hardening and hence α_{ij} are identically equal to zero.

The plastic strain increments are given by the normality condition

$$d\varepsilon_{ij}^p = d\lambda \frac{\partial F}{\partial \sigma_{ij}} \tag{2-27}$$

where $d\lambda$ is a scalar plastic parameter. Following the standard procedure used in plasticity theory, an incremental stress-strain relation in matrix form can be derived from Eqs. (2-24) to (2-27) as

$$\{d\sigma\} = [C_{ep}]_s \{d\varepsilon\} \tag{2-28}$$

Where $[C_{ep}]_s$ is incremental elastic-plastic constitutive matrix.

2.3 Reinforcement Interaction Effects

The interaction effects between the reinforcement and concrete have generally been modeled in three different ways. These are: (1) the discrete approach, (ii) the embedded approach, and (iii) the smeared approach. In the discrete approach, the concrete and reinforcement steels are treated as separate homogeneous continua having different constitutive models as described in the previous sections. For example, in finite element applications, the concrete and reinforcing bars are discretized into separate finite elements interconnected at nodal points. Special interface (bond-link) elements are often used to model local interaction effects such as dowel shear, tensile crack growth and aggregate interlock.

In the embedded approach, the reinforcing bars are represented as axial members built into the concrete elements. The bars, which can be arbitrarily oriented in the concrete elements, are subjected to the same displacement field as the concrete elements in order to ensure compatibility. Thus, a perfect bond between the steel and the concrete is assumed.

The above two approaches, however, require a large number of elements to model a structure. This is due to the fact that every reinforcing bar must be considered individually. Hence, these methods can only be used for analyzing simple structural members, e.g., beams, panels, etc. For general reinforced concrete structures, the distributed or smeared approach has been adopted by most researchers, not only because it leads to computationally efficient finite element models, but also because it can be easily incorporated into the existing computer codes. In this method, the reinforcing bars are distributed (smeared) in the concrete element resulting in a locally homogeneous continuum. The constitutive stress-strain matrix of the homogenized continuum is obtained as a function of the concrete and steel material properties. Various smearing (and desmearing) procedures have been used by different analysts. A set of mathematically consistent procedures that have been adopted by BNL are briefly described as follows.

Let σ_i^k and ε_i^k, i = 1, 2, ..., 6 be the stress and strain components in the kth component material, respectively. The constitutive relations are

$$\{\sigma^k\} = [C^k]\ \{\varepsilon^k\} \tag{2-29}$$

Equation (2-29) can represent either a linearly elastic stress-strain law or a nonlinear stress-strain law. In the case of elastic-plastic deformation, the total quantities σ^k and ε^k are replaced by their incremental values, and C^k is viewed as the corresponding elastic-plastic material matrix. Let the overall average stresses and strains in the composite structure be denoted by $\bar{\sigma}_i$ and $\bar{\varepsilon}_i$, i = 1,2,---,6. The stresses and strains in the component materials, i.e., concrete and steel, are partitioned into two sets: Set I consists of those strain components that are uniform in the constituents, i.e.,

$$\{\varepsilon_i^k\} = \{\bar{\varepsilon}_I\} \tag{2-30}$$

and Set II consists of the remaining stress components that are uniform

$$\{\sigma_{II}^k\} = \{\bar{\sigma}_{II}\} \tag{2-31}$$

Corresponding to the above partitioning of the stresses and strains, the following smearing (or averaging) equations are used

$$\{\bar{\sigma}_I\} = \sum_{k=1}^{2} \nu^k [A^k] \{\sigma_I{}^k\} \tag{2-32}$$

$$\{\bar{\varepsilon}_{II}\} = \sum_{k=1}^{2} \nu^k [B^k] \{\bar{\varepsilon}_{II}{}^k\} \tag{2-33}$$

where ν^k is the volume fraction of the kth material, and A^k and B^k are coefficient matrices which account for the geometric shape factors of the reinforcements.

Based on the above assumptions, the effective stress and strain relations, whether linear or nonlinear, can then be derived in terms of the material matrices of the component materials, i.e.,

$$\{\bar{\sigma}\} = [C] \{\bar{\varepsilon}\} \tag{2-34}$$

Detail derivation of $[\bar{C}]$ matrix and application of this method can be found in Ref. [15].

In order to find the stresses in the individual steel and concrete materials, a desmearing procedure (which is essentially the inverse of the smearing procedure) must be applied. The details for this are also given in Ref. [15].

2.4 Prestressing

In order to offset the limited strength of concrete in tension, prestressing has been used in the design and construction of some containment structures. One difficulty in analyzing prestressed structures involves the determination of the loss of prestress, which results from: (1) the elastic shortening of the concrete, (2) the friction between the tendon and the concrete, (3) creep and shrinkage of the concrete, and (4) the stress relaxation in the prestressed tendons. An exact evaluation of these effects

is very complex and is usually not carried out. The combined effect of the mechanisms mentioned above is generally approximated by a specified reduction in the original prestress tendon loads.

In the finite element methodology, tendons can again be modeled by either the discrete, the embedded or the smeared approach described previously. BNL has used both the discrete and the smeared approaches for a containment evaluation carried out under this program (Section 3.4.1).

2.5 Geometric Modeling

The geometric and reinforcement details of the concrete containments are inherently very complex. Exact modeling of these details is presently beyond the state-of-the-art, and hence various idealizations have been employed by analysts in their computer models. The most commonly used idealizations and their impact on the analysis results are discussed below.

2.5.1 Containment Geometry

Most investigators have assumed the containments to be axisymmetric for analyzing the gross structural failure behavior under internal pressure loadings. The effects of various penetrations (personnel and air locks) and thickness variations in the circumferential directions (e.g., in the vicinity of anchorage buttresses, etc.) have been ignored. This has usually been justified on the ground that these geometric changes are "local" or small compared to the overall size of the containment, and therefore they would not significantly affect the global structural response. Additionally, since the minimum wall thickness in the circumferential direction is generally used in the analysis, the predicted results would tend to be conservative. It is also pointed out that the areas surrounding the penetrations are unlikely to experience local failure since they are usually more heavily reinforced when compared to the rest of the containment. A limited number of local stress analyses[7,17] have been carried out to verify this assumption.

Steel reinforcements and tendons (for prestressed containments) are similarly assumed to be axisymmetric. In reality, only the hoop reinforcements in the cylindrical wall are close to being axisymmetric. Other reinforcements and tendons are smeared in the circumferential direction which makes them axisymmetric only in a distributed (i.e., average) sense. The smearing approach, which is used extensively for modeling of composite materials, is considered to be acceptable because the circumferential rebar spacings are quite small when compared to the containment size. Thus, local circumferential stiffness variations are not expected to change the structural behavior appreciably.

2.5.2 Basemat Restraint

In some containment analyses, the basemats have either not been modeled[2], or have been assumed to be restrained[12,16,18] at the basemat - soil interface. This is a reasonable assumption for containments designed for low internal pressure since for these containments the basemat uplift under the pressure loads would not be appreciable[12]. For containments with high design pressures, however, the basemats may be subjected to significant uplift before the containment failure. The resulting basemat displacements would affect the stresses at the basemat-cylinder intersection which, as mentioned earlier, is one of the potential failure locations. The effect of basemat uplift was assessed in a recent finite element analysis for the Main Yankee Containment building[8]. The structural responses were found to be similar up to 73 psig internal pressure with or without the basemat restraints, but they differed substantially at higher pressures. When basemat uplift was allowed, failure due to severe concrete damage at the intersection was predicted at 96 psig. Without the basemat uplift, however, failure due to general yielding of the hoop rebars in the vicinity of the cylinder mid-section was estimated at 118 psig.

2.5.3 Finite Element Mesh

Containment models based on various types of finite elements have been used for the geometric idealization. Most of these models can adequately predict the containment failure responses governed by high membrane stresses.

In particular, the models would give reasonably good estimates of the failure pressures if the containment failure is initiated by the yielding of hoop reinforcements (and tendons) in the cylindrical wall. For this failure mode even the results from simple hand calculations are found to be sufficiently accurate. However, some of the simplified finite element models would be clearly deficient for describing the failure behavior governed by severe bending and shear deformations. Containments are indeed subjected to such deformations at the points of discontinuity, e.g., at the basemat-cylinder intersection. Thus, shell-type finite elements, because of the limitations in their assumed displacement fields, are not suited to model the complex interactions between out-of-plane (radial) shear forces and bending moments. Furthermore, in order to model potential shear failure it is necessary to use several layer of finite elements through the wall thickness. Simple containment models that use only one or two layer of elements, regardless if they are shell elements[17,19] or two dimensional axisymmetric elements[2,16,18], they would not properly describe the stress and strain fields occurring under progressive shear failure.

2.5.4 Rebar Locations

Due to various simplifications in the geometric discretization, rebar locations in the containment walls have often not been modeled accurately. In a number of containment analyses[2,8,16] the inner meridional rebars have been assumed to be located at the inside face of the containment walls. This approximation leads to an overestimation of the bending stiffness of the walls since the rebars are now subjected to higher strains under bending action. At the basemat-cylinder intersection, a higher bending stiffness would reduce cracking of the concrete through the wall thickness. This in turn would reduce the loss of shear stiffness of the concrete (see Eqs. 2-18 and 2-19), and thus result in a higher shear capacity of the wall section. It should be noted that the error in modeling rebar locations would not appreciably affect

the membrane stresses and, consequently, ultimate pressures for failure governed by membrane stresses[12] (e.g., yielding of hoop rebars). For the prediction of shear failure mode however, close attention to reinforcement details must be given, especially with regards to meridional rebars near the basemat-cylinder intersection.

2.5.5 Rebar Orientations

In most containment finite element analyses, the rebars have been modeled by truss or ring (for hoop rebars) finite elements. When truss elements are used, the placement and orientation of the rebars are defined by the two end nodes of the trusses. Effective reinforcement ratios are specified by the cross-sectional areas of the truss elements. This approach works well for modeling the meridional rebars in the containment cylinder, where these bars essentially vertical and their effective reinforcement ratios change only at specific elevation levels. However, since the orientation of truss elements is limited by available nodes in a finite element grid, more general rebar patterns cannot be easily modeled. For example, in an axisymmetric containment model, all truss elements are confined to a two-dimensional plane of the finite element grid. Consequently, out-of-plane orientations of the complex patterns of rebars normally used in the dome, and that of seismic (diagonal) rebars in the cylinder, cannot be accurately represented. Even the orientations of in-plane reinforcements that are not parallel to the meridian, e.g., secondary meridional rebars, shear ties, etc., are not easily defined. In an axisymmetric model, the use of truss elements in the dome suffer from another disadvantage. In order to maintain a specified reinforcement ratio in a unit radian segment of the dome, the truss cross-sectional area must be continuously varied along the dome's meridian. This is difficult to achieve, especially near the dome apex, since the number of truss elements is fixed by the finite element mesh. It should further be noted that the same problems are also encountered when prestressing tendons are modeled by truss elements. Indeed, these modeling limitations may have led to, respectively, a premature yielding of rebars and tendons, and an unconventional deformation pattern near the apex of the dome in two prestressed containment analyses presented in Ref. [7] and [18].

When the rebars and tendons are modeled by the smearing approach (Section 2.3), their orientations and effective reinforcement ratios can be defined arbitrarily. This is one of the reasons that this approach has been adopted in the BNL failure evaluations presented in this report. Its application for a reinforced concrete containment has been demonstrated previously in Ref. [12].

3. COMPARATIVE CONTAINMENT ANALYSES

As discussed in the previous section, a variety of finite element models with different material and geometric idealizations have been used to study the failure behavior of concrete containments. Therefore, it is to be expected that these would cause some variations in the analysis results. One of the major purposes of this study was to perform independent failure analyses for selected containments and to compare the predicted results with those presented in the literature. The containments chosen for the comparative evaluations were those of the Indian Point (Unit 3) and Zion reactors. The reason for selecting these containments was that their failure responses have been investigated in detail in several studies[2,7,16,17] and various conflicting results have been presented. The analysis results are different not only in their estimates of the final failure pressures but also in the predictions of the failure modes. In the following sections, results obtained from BNL finite element analyses for the two containments are discussed along with those obtained in previous studies.

3.1 Indian Point Containment (Unit 3)

The Indian Point (Unit 3), Containment Building (see Fig. 5) is a reinforced concrete structure consisting of three basic parts: (1) a basemat, (2) a right circular cylinder, and (3) a hemispherical dome. The basemat is essentially a 9' thick circular slab which supports the cylinder and other internal structures. The 4'6" thick cylindrical wall, has an internal diameter of 135' and a height of 148' as measured from the top of the basemat to the springline. The cylinder is capped by the dome which is 3'6" thick and has the same internal diameter (135') as the cylinder. Thus, the total height of the containment building above the basemat is 219'.

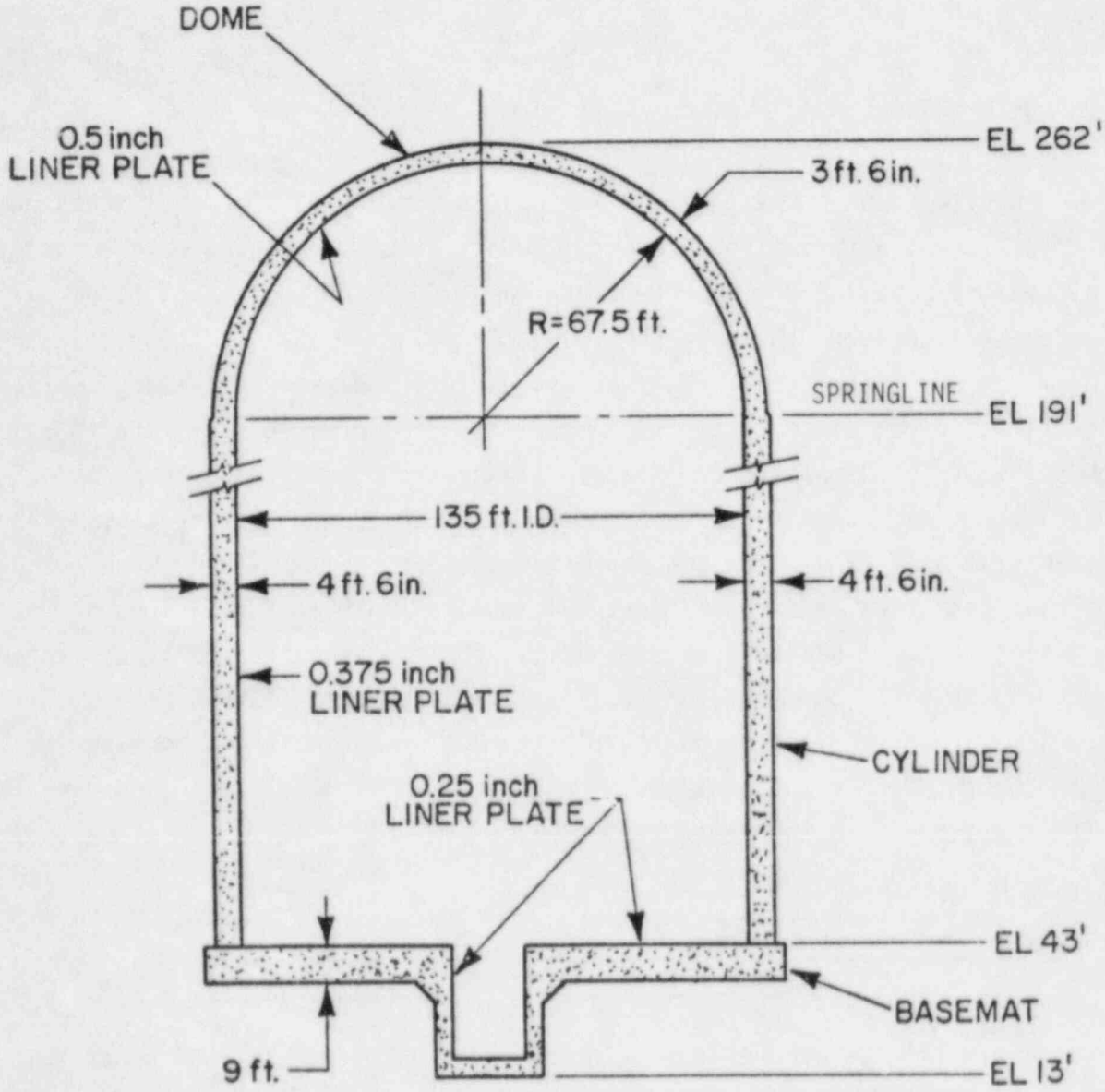

Figure 5. Indian Point Containment Building

The interior surface of the containment is lined with a ductile steel liner whose thickness is 1/4" over the basemat, 1/2" in the dome section and in the bottom 30' section of the cylinder, and 3/8" over the remaining height of the cylinder. Other basic dimensions and features of the containment are shown in Fig. 5.

The containment is reinforced with Grade 60 (nominal yield stress 60 ksi) reinforcing bars of various sizes (mainly #18, #14 and #11). The primary membrane reinforcement in the cylindrical wall and dome is divided into two equal groups placed near the inside and outside faces of the containment wall. Each group consists of two layers of hoop bars and one layer of meridional bars as shown in Fig. 6. A layer of helical bars at +45° with the vertical axis is placed near the outside face to resist in-plane seismic forces. These bars extend form the top of the basemat to bottom third of the dome. In addition, since the basemat-cylinder intersection is subjected to high bending moments and shear forces, secondary meridional reinforcement (Fig. 6) is provided in this region. The major reinforcement details for the containment wall are summarized in Table 1 and 2. Further information pertaining to the containment geometry and reinforcements can be found in Ref. [20].

3.1.1 BNL Indian Point Containment Model

The BNL finite element model of the Indian point containment was developed using the NFAP[21] (Nonlinear Finite Element Analysis Program) computer code. The model, shown in Fig. 7, is based on an axisymmetric idealization of the geometry which, as discussed in Section 2.5, is a good approximation for the failure analysis under axisymmetric pressure loads. The containment model consists of 408 eight-noded isoparametric elements and a total of 1399 nodes. In addition, a set of nonlinear spring elements (high stiffness in compression and zero stiffness in tension) were used under the basemat in order to model the soil restraint while allowing possible uplifting of the basemat. As shown in the figure, the model has 8 layers of elements in both the cylindrical wall and the hemispherical dome, and 6 layers in most of the basemat. The element layers were chosen to represent separately the liner, the plain concrete, and the reinforced concrete with different reinforcing bars. Particular attention was given to selecting the spacings

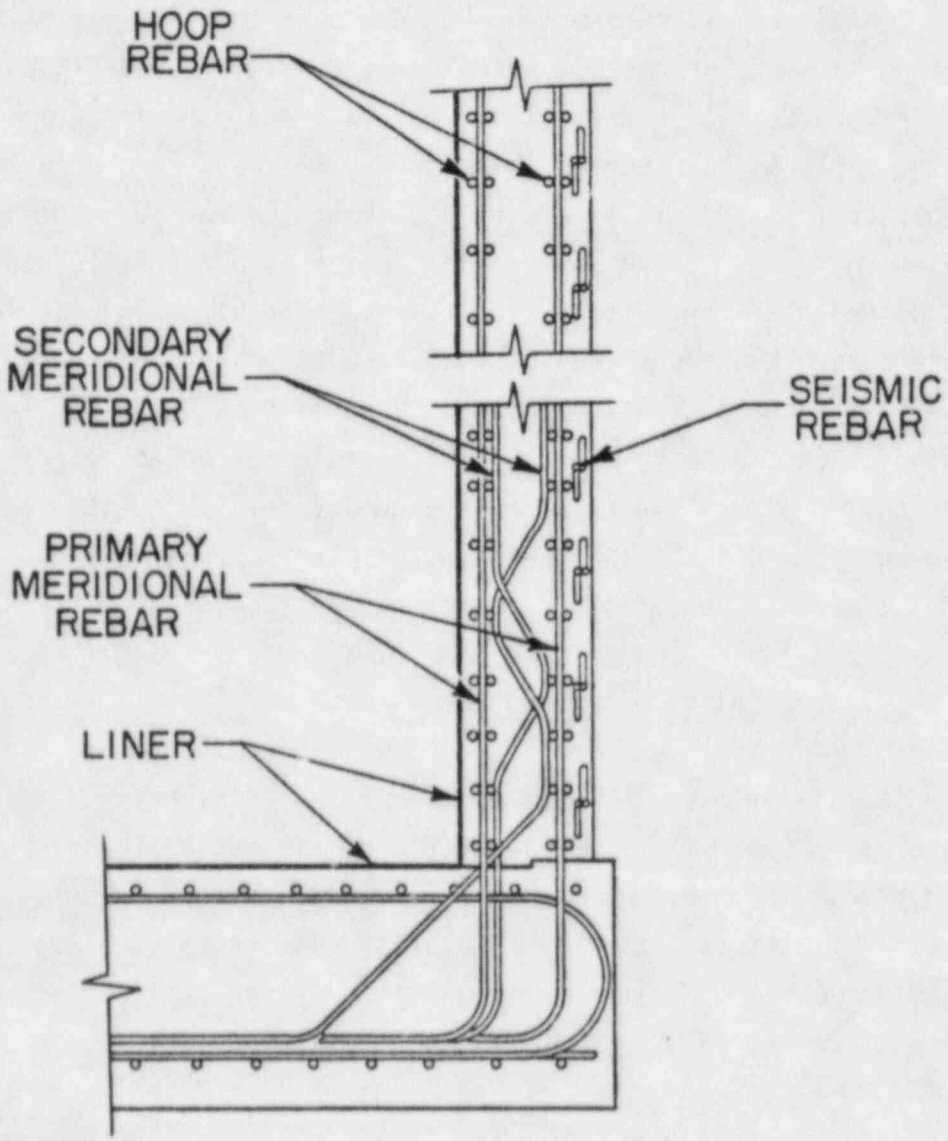

Figure 6. Reinforcements in the Indian Point Containment Cylinder

Table 1. Reinforcement Details of the Indian Point Containment Cylinder.

Elevation	Hoop (Both Faces)	Meridional (Both Faces)		Seismic Diagonal
		Primary	Secondary	
43' ~ 68'	2 - #18 @ 14"	#18 @ 12"	#18 @ 12"	#18 @ 30"
68' ~ 88.5'	2 - #18 @ 14"	#18 @ 12"	#11 @ 12"	#18 @ 30"
88.5' ~ 93.25'	2 - #18 @ 14"	#18 @ 12"	2 - #11 @ 36"	#18 @ 30"
93.25' ~ 97.8'	2 - #18 @ 14"	#18 @ 12"	#11 @ 36"	#18 @ 30"
97.8' ~ 153.5'	2 - #18 @ 14"	#18 @ 12"	None	#18 @ 30"
153.5' ~ 191'	2 - #18 @ 14"	#18 @ 12"	None	#18 @ 60" #14

Table 2. Reinforcement Details of the Indian Point Containment Dome.

Angle From Spring Line	Hoop (Both Faces)	Meridional (Both Faces)	Seismic Diagonal
0° ~ 9.5°	#14 @ 8.25"	#18 @ 0.8°	#18 @ 4° #14°
9.5° ~ 18.5°	#14 @ 8"	#18 @ 0.8°	#18 @ 12" #14
18.5° ~ 35°	#14 @ 8"	#18 @ 0.8°	#11 @2°
35° ~ 55°	#14 @ 8"	#18 @ 0.8°	None
55° ~ 60°	#14 @ 8"	#18 @ 0.8°	None
60° ~ 75°	#14 @ 8"	#18 @ 1.6°	None
75° ~ 83°	#14 @ 8"	#18 @ 3.2°	None
83° ~ 86°	#14 @ 8"	#18 @ 6.4°	None
85° ~ 90°	#14 @ 8"	#18 @ 12.8°	None

and sizes of the layers in order to model the actual rebar placements as closely as possible. As mentioned previously, it is necessary to model the rebar locations accurately for the prediction of a potential shear failure near the basemat-cylinder intersection where high bending moments and shear forces are developed. Further, a finer mesh of elements was used for modeling the intersection region because of the expected higher stress and strain gradients.

The inelastic behavior of the plain concrete was described by the Chen and Chen elastic-plastic-fracture model. Material parameters required for this model were estimated from as-built properties of the concrete and are given as follows.

Material parameters for the concrete:

Young's modulus = 3,700 ksi
Poission's ratio = 0.19
Yield strength in uniaxial tension = 0.216 ksi
Yield strength in uniaxial compression = 1.8 ksi
Yield strength in biaxial compression = 2.160 ksi
Fracture strength in uniaxial tension = 0.4 ksi
Fracture strength in uniaxial compression = 4.0 ksi
Fracture strain in tension = 0.000125
Fracture strain in compression = 0.003

For modeling the post-cracking behavior of concrete, the normal stiffness reduction factor, α in Eq. (2-14), was taken to be 0.0001 during the element stiffness calculation phase. A negative value of -0.1 was used for element stress calculations for modeling the tension stiffening effect. The shear stiffness of the cracked concrete was obtained from Eqs. (2-18) and (2-20) in which the constant c was assumed to be 0.5.

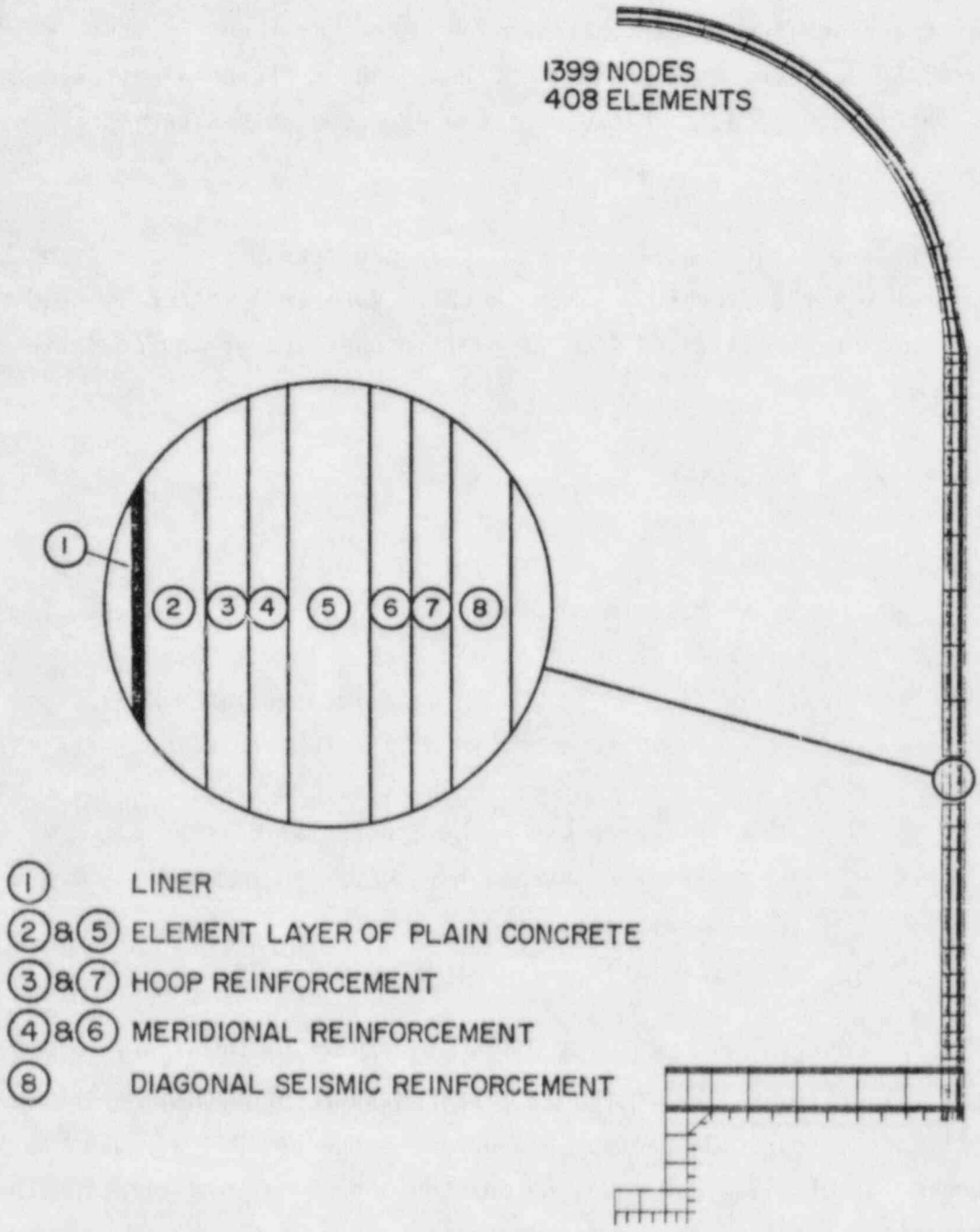

Figure 7. BNL Indian Point Containment Model

Elastic-plastic behavior of the reinforcing bars and liner steels was modeled by a bilinear stress-strain curve and a von Mises plasticity model with isotropic hardening. Young's modulus of elasticity, plastic tangent modulus and Poission's ratio were taken to be 29,000 ksi, 100 ksi and 0.3, respectively. As-built values for the mean yield strengths, 48.4 ksi for the liner, and 69.7 to 71.0 ksi for various rebars, were used.

A composite material formulation described in Section 2.3 was used for modeling the inelastic material behavior of reinforced concrete layers. Sets of uniform strain and stress components in Eqs. (2-29) and (2-30) were defined by assuming that the normal strain component along the reinforcement (say, ε_1) and all stress components except the one along the reinforcement (σ_2, σ_3, τ_{12}, τ_{21}, τ_{13}), were uniform in both the concrete and steel. Thus, the material matrix [c] in Eq. (2-33) was first obtained in a local coordinate system associated with the reinforcement direction, and was subsequently transformed to the global coordinate system.

3.2 BNL Analysis Results for the Indian Point Containment

The loads considered in the analysis were the dead-weight or gravity loads and internal pressure. The entire gravity loads were applied to the containment in the first load step at the beginning of the analysis. The internal pressure was, however, incrementally applied. The pressure increments were 1 psig following the onset of nonlinear response. Large displacement effects on the element stiffnesses and pressure loads were taken into account during the nonlinear solution phase. In the nonlinear range, a Newton-Raphson procedure with stiffness reformation for each equilibrium iteration was used to obtain convergent solutions.

3.2.1 Deformation Response

Undeformed and deformed (before failure) shapes of the containment are depicted in Fig. 8. For clarity, the displacements for the deformed shape are multiplied by a factor of 50. The figure shows large bending deformations at

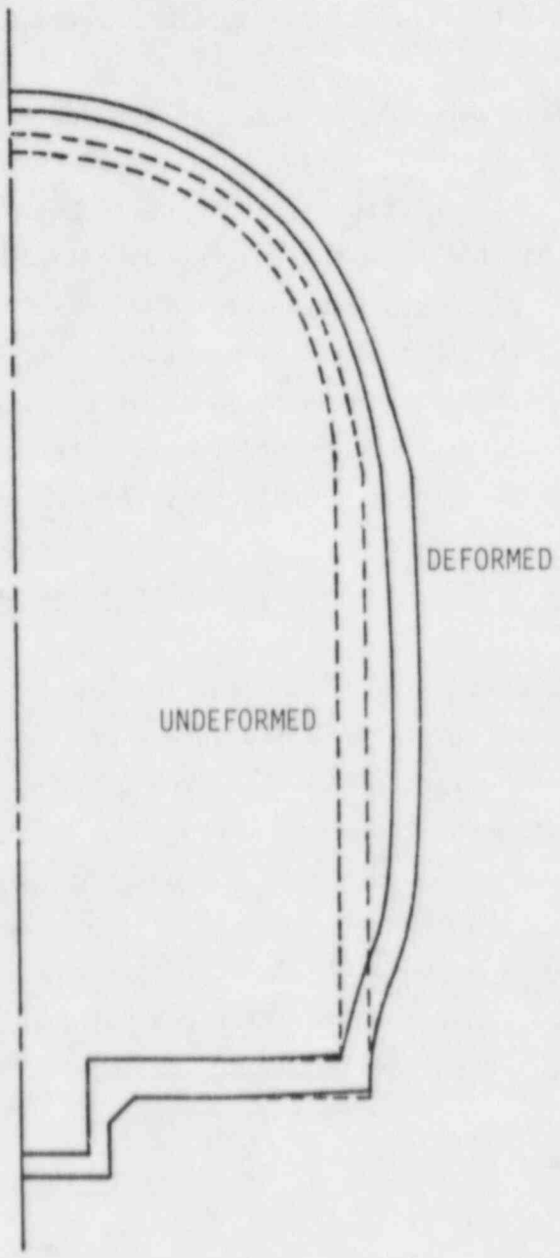

Figure 8. Undeformed and Deformed Shapes of the Indian Point Containment

the basemat-cylinder intersection, and comparatively large radial displacements in the middle of the cylindrical wall. The deformations of the basemat indicate that up-lifting occurs below the cylindrical wall near the intersection.

The growth of the deformation field is illustrated in Fig. 9 where radial displacement at mid-cylinder and vertical displacement at the top of the dome are plotted versus internal pressure. As can be seen, the displacements are small until tension cracks develop in the concrete at internal pressures between 25-33 psig (see below). The displacements then grow more rapidly as the concrete loses its load carrying capacity. The rates at which these displacements increase are then controlled by the stiffnesses of the steel members and by the tension-stiffening effect of the cracked concrete.

3.2.2 Cracking and Shear Failure of Concrete

Vertical cracks due to hoop stresses first appear in the middle of the cylindrical wall at 25 psig. The cracks spread quickly with increasing pressure covering almost the entire length of the cylinder at 26 psig. Only small section above the basemat-cylinder intersection remain uncracked. The hoop strains are very low in this region due to the radial constraints provided by the basemat. As the pressure increases to 29 psig, perpendicular cracks due to both hoop and meridional stresses are initiated in the entire section of the dome.

The next set of cracks appear at the basemat-cylinder intersection when the pressure reaches 33 psig. These cracks are caused by high meridional and shear stresses in the elements at the inside of cylindrical wall. The cracks are formed at some angles from the horizontal plane because of the combined effect of meridional and shear stresses. The cracking progresses through the intersection with increasing pressure, reaching the middle of the intersection (i.e., the cylindrical wall thickness) at 48 psig. At this pressure, horizontal cracks due to meridional stresses also appear in the entire cylindrical wall except at the outside of the wall near the intersection. The concrete in

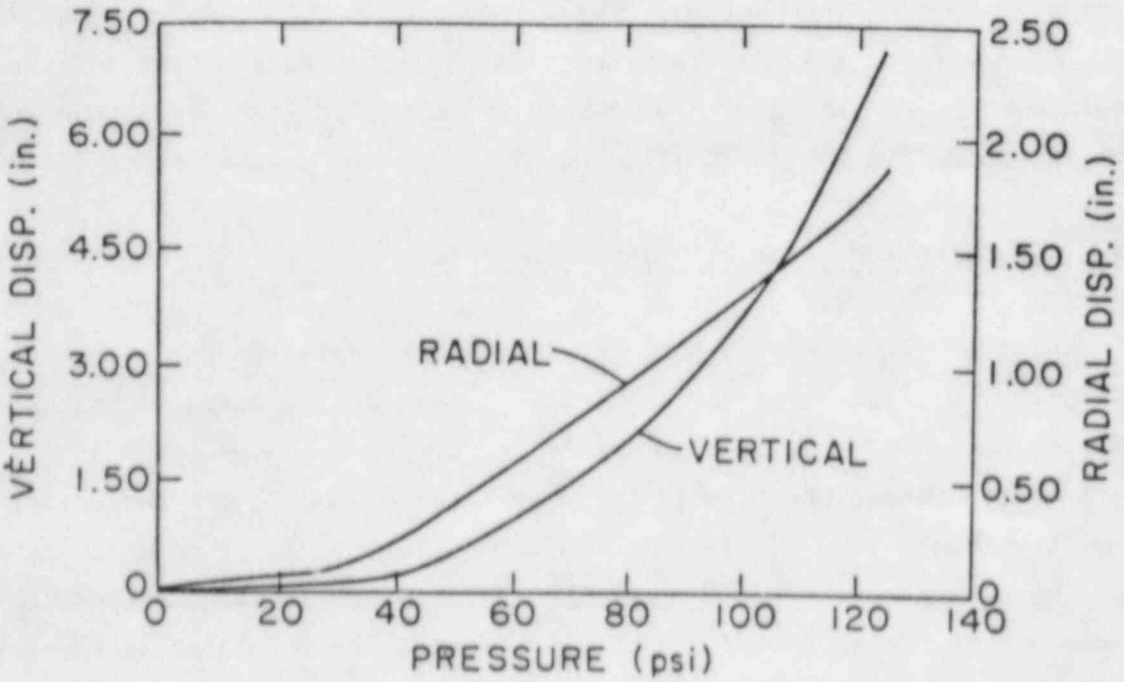

Figure 9. Radial Displacement at Cylinder Mid-Height and Vertical Displacement at Dome Apex Versus Pressure (Indian Point Containment)

this region is under compression because of the bending deformations. As the internal pressure is increased further from 48 to 77 psig, the cracked regions expand slowly but essentially with the same crack configurations. Above 77 psig, high shear stresses at the basemat-cylinder intersection introduce another set of secondary cracks in this region. When this occurs, the concrete is assumed to fail in shear and its shear stiffness is greatly reduced. In the present analysis, ten percent of the uncracked shear stiffness is retained in order to approximately represent the cumulative effect of interface shear transfer, dowel mechanism and the stiffness contributions from the reinforcement ties and stirrups.

Shear failure of the concrete progresses through the wall with increasing pressure. At 110 psig, 50 percent of the intersection has failed in shear. The extensive cracking relieves some of the bending moment and shear force in this region. The depth of shear failure, however, keeps increasing, reaching the outside face meridional bars (72 percent of the wall thickness) at 125 psig. Above this pressure (i.e., at 126 psig), a convergent numerical solution could not be obtained. This indicates that the basemat-cylinder intersection cannot carry any further increase in the load.

It should be noted that the numerical divergence of the solution is not caused by large displacements which would occur when the rebars have substantially yielded. Shear failure is not necessarily preceded by large deformations. This is indeed the situation encountered in the present analysis. Because of the loss of shear capacity of the concrete at the intersection which has suffered multiple cracking, the elements in this region cannot absorb further shear forces. This failure is therefore an actual phenomenon and is not due to artificial numerical instabilities.

Plasticity of concrete in compression is initiated at 110 psig in some elements at the cylinder base on the outer surface. The plastic zone spreads to neighboring elements with increasing pressure. However, the effective stress in all these elements remains considerably below the fracture strength of the concrete in compression (4 ksi) even at the peak pressure of 125 psig.

3.2.3 Liner and Rebar Stresses at Basemat-Cylinder Intersection

Meridional stresses in both the liner and inside vertical rebars at the basemat-cylinder intersection are depicted in Fig. 10. These stresses grow linearly at a slow rate until the concrete begins to crack at 29 psig. The stresses then grow rapidly with pressure as the cracks progress through the wall and the concrete meridional loads are transferred to the steel members. At 84 psig, 7 psig above the pressure at which a second set of cracks develop at the intersection (77 psig), the liner becomes fully plastic. Additional meridional stresses above 84 psig pressure are carried mainly by the inside vertical rebars, and to some extent by the small section of intact concrete. As shown in the figure, the rebar stresses grow at an even higher rate after the liner has become plastic. Finally, the rebars become plastic at 120 psig. This is soon followed by the shear failure at the intersection at 126 psig as discussed previously.

3.2.4 Liner and Rebar Stresses at Cylinder Mid-Height

Hoop stresses in the containment are greatest at the cylinder mid-height at an elevation of 114 ft. For a section at this elevation, hoop stress versus internal pressure curves for the liner, hoop rebars and diagonal rebars are plotted in Fig. 11. The stresses in all the steel members are low until the onset of cracks due to hoop stresses at 25 psig. Above this pressure and up to 104 psig, the stresses grow almost linearly with increasing pressure. Note that the hoop stress in the liner, because of the multi-axial stress state, is higher than that in the hoop rebars in this pressure range. Also, the hoop stress in the diagonal rebars is much lower (approximately 25 percent) since they are inclined 45° to the horizontal axis.

The liner becomes plastic at 104 psig under combined hoop and meridional stresses. Additional hoop stresses are then transferred to the hoop and diagonal rebars resulting in higher growth rates of hoop stress versus pressure. Both the hoop and diagonal rebars, however, remain elastic up to 125 psig internal pressure. Analysis results could not be obtained above this pressure because of the shear failure at the basemat-cylinder intersection.

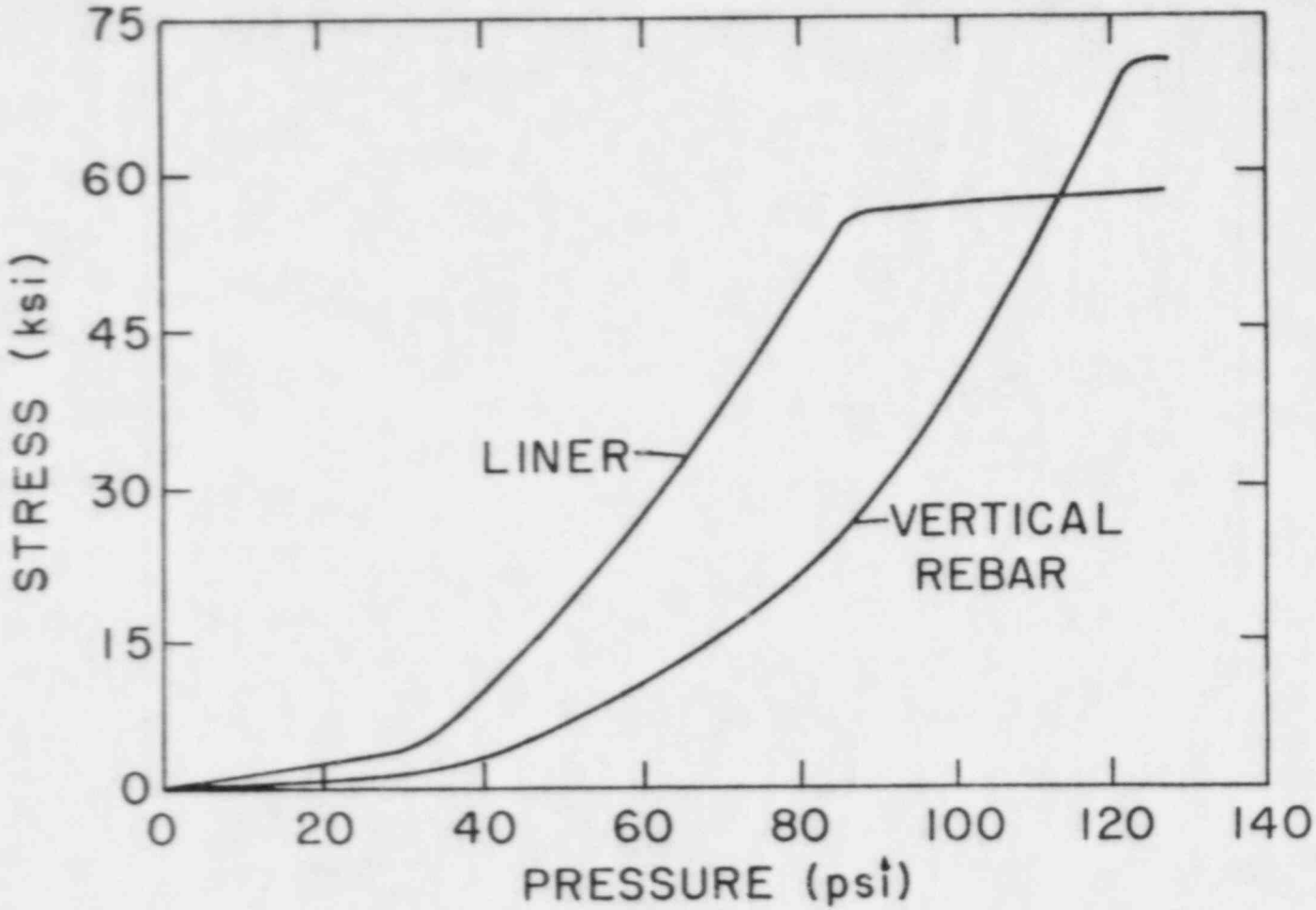

Figure 10. Meridional Stresses in the Liner and Inside Vertical Rebars Versus Pressure (Indian Point Containment)

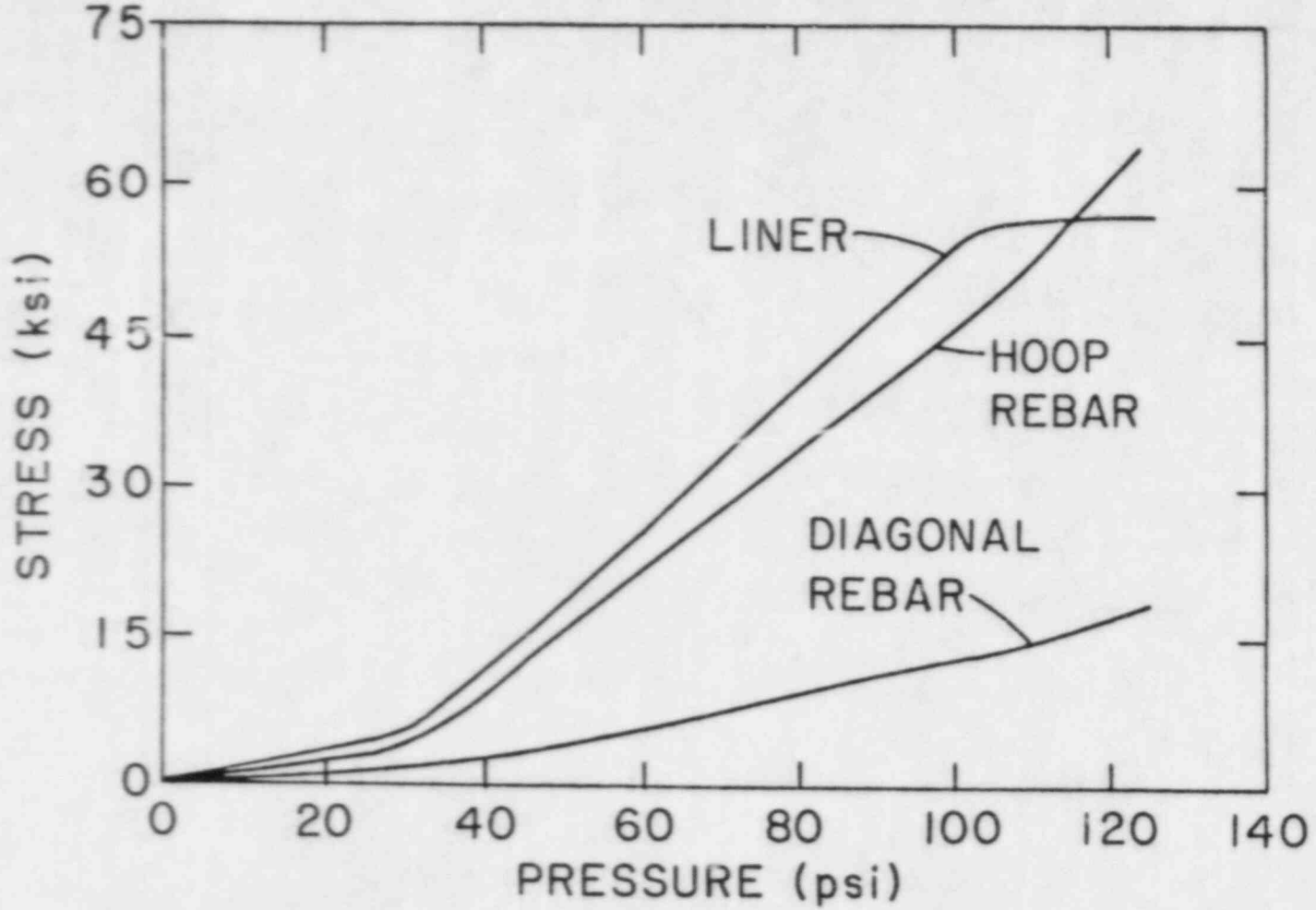

Figure 11. Hoop Stresses in the Liner, Hoop Rebars and Diagonal Rebars Versus Pressure (Indian Point Containment)

3.3 Previous Analysis Results for the Indian Point Containment

Failure response of the Indian Point Containment Building under accident pressures has previously been investigated by Von Riesemann, et al.[22] at Sandia National Laboratories (SNL), by Butler and Fugelso[7] at the Los Alamos Scientific Laboratory (LASL), and by Fardis, et al.[2] at the Massachussetts Institute of Technology (MIT). Axisymmetric finite element results obtained at SNL show that the radial displacement of the containment wall at a point 16 feet below the springline becomes unbounded at a pressure of 151 psig. The analysis apparently does not predict a shear failure at the basemat-cylinder intersection. Results for stress distributions in the concrete and rebars are however not presented in Ref. [22] to allow for a comparative evaluation. Therefore, the following discussion is limited to the analyses carried out at LASL and MIT.

3.3.1 LASL and MIT Containment Models

LASL Finite Element Model - This axisymmetric finite element model was developed using the general purpose nonlinear finite element code, ADINA[6]. The two-dimensional model (Fig. 12) idealized the structure by using four layers of axisymmetric elements to model the cylindrical wall and dome, and two layers of these elements for the basemat. An additional thin layer of shell elements was used to model the liner. Nonlinear spring elements were used under the basemat to represent the soil stiffness. These springs were assigned a zero tensile stiffness, which in essence allowed the basemat to uplift without a boundary restraint. The reinforcement bars were modeled by ring and truss finite elements. A perfect bonding between the steel and concrete was assumed to occur at the element nodes.

One of the nonlinear material models available in ADINA (see Section 2.1.1) was used to model the inelastic behavior of plain concrete. The following material properties were assumed: tangent modulus of elasticity at zero strain = 3,700 ksi, Poisson's ratio = 0.19; uniaxial cutoff tensile stress = 0.4 ksi, uniaxial maximum compressive stress = 4 ksi; corresponding uniaxial compressive strain = 0.002; uniaxial ulimate compressive stress = 2.9 ksi; corresponding ultimate compressive strain = 0.003. In the cracked concrete, normal and shear stiffness reduction factors of 0.0001 and 0.5, respectively, were employed. For the steel members, a bilinear stress-strain

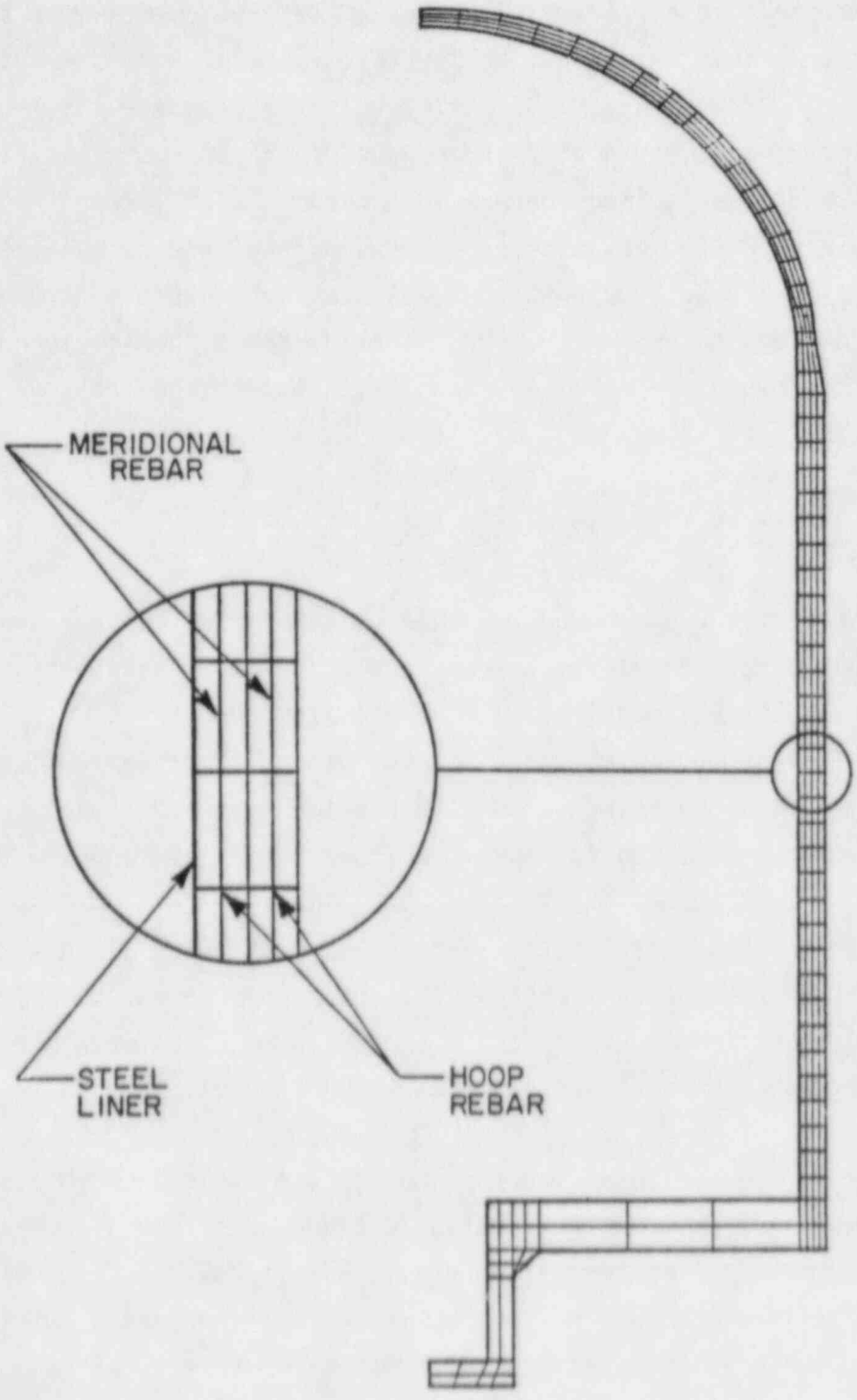

Figure 12. LASL Indian Point Containment Model (Ref. 7)

approximation for the uniaxial response with elastic and plastic tangent moduli of 29,000 ksi and 0.29 ksi, respectively, were used. As-built values for mean yield strengths were assumed in the analysis.

MIT Finite Element Model - A modified version of the nonlinear finite element code ANSR-1[23] was used at MIT to carry out the axisymmetric analysis for the containment. The basemat was considered to be rigid and was not included in the model. The containment wall was assumed to be fixed at the bottom. The model consisted of two types of element, namely, axisymmetric quadrilateral elements for the concrete and one dimensional axisymmetric membrane elements for the steel liner and reinforcing bars. As shown in Fig. 13, only one layer of quadrilateral elements was used across the wall thickness. The membrane elements were placed on the inside and outside faces of the quadrilateral elements.

The concrete was modeled as a linear elastic orthotropic material with elastic moduli that depended on the sign of normal strain in the orthotropic directions. The elastic modulus was taken to be 3000 ksi for the concrete in compression and 3 ksi for the tension-cracked concrete. The effect of aggregate interlock and dowel action on the shear rigidity of concrete, was modeled by Eq. (2-19). The nonlinear material behavior of the steel liner was represented by an associative incremental von Mises material model with a constant, i.e., perfectly plastic, yield surface. Uniaxial stress-strain response of the rebars was idealized by Eq. (2-23).

3.3.2 LASL and MIT Analysis Results (Indian Point Containment)

LASL Analysis Results - Analysis results from the LASL model show that extensive cracking occur due to hoop stresses between 30 - 40 psig internal pressure. Radial displacement at cylinder mid-height (Fig. 14) show constant structural stiffness in the hoop direction before and after this hoop cracking. As the internal pressure increases, concrete cracking becomes more widespread, especially at the basemat-cylinder intersection. At 54 psig, the base of the cylindrical wall is cracked perpendicular to the meridional direction from combined tensile and shear forces. Additional cracks are initiated perpendicular to these cracks on the inside surface of the wall as the internal pressure increases to 70 psig.

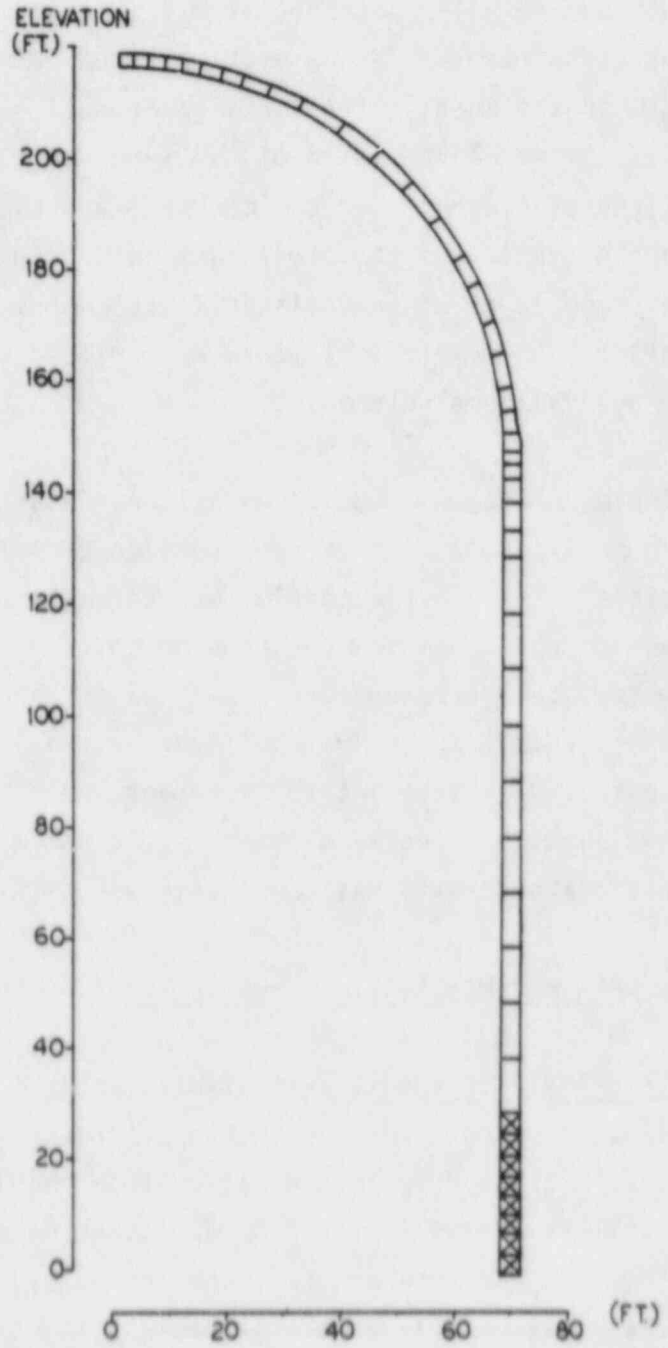

Figure 13. MIT Indian Point Containment Model (Ref. 2)

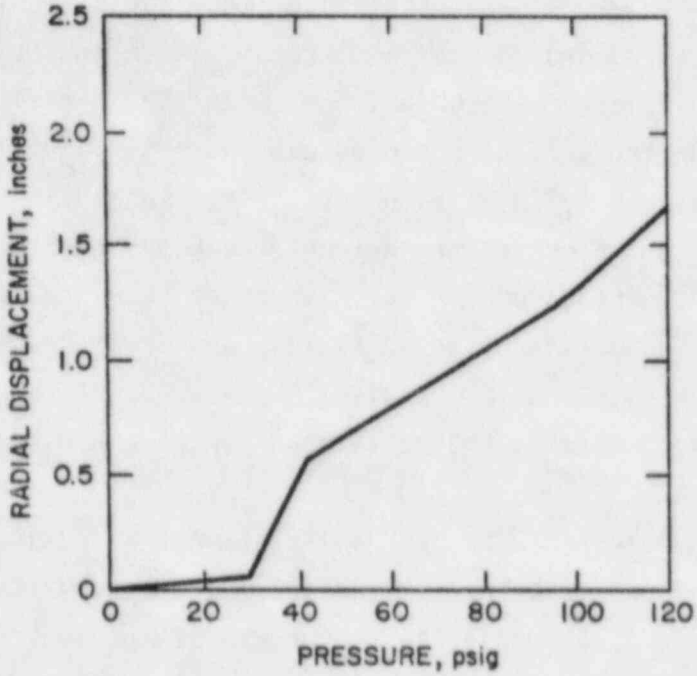

Figure 14. Radial Displacement at Cylinder Mid-Height - LASL Analysis for the Indian Point Containment (Ref. 7)

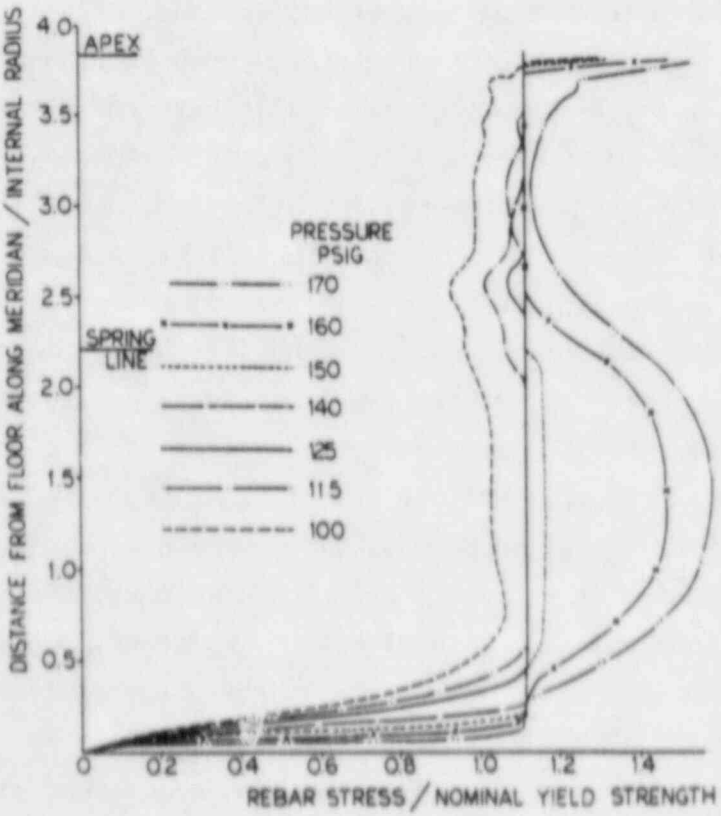

Figure 15. Stresses in the Inside Hoop Rebars - MIT Analysis for the Indian Point Containment (Ref. 2)

With perpendicular cracks in two planes, the concrete is assumed to have failed in shear. However, because of ADINA code limitations, shear strength of the concrete is reduced only by 50 percent, which in the analytical model allows it to carry additional shear forces. The shear failure nevertheless progresses through the wall as the pressure increases. At 118 psig, 75 percent of the basemat-cylinder intersection has failed in shear. In addition, significant crushing of the concrete under high compressive stresses takes place on the outside of the wall. Further increase in the internal pressure results in additional shear failure and compression crushing, and eventually the numerical solution fails to converge. Internal pressure of 118 psig is then projected to be the containment failure pressure.

MIT Analysis Results - The MIT finite element analysis predicts the critical region of the containment to be at the middle half of the cylinder in the hoop direction. The initiation and growth of the concrete cracks are not discussed, presumably because the concrete has already cracked due to initial thermal stress which are taken into account in this analysis. The finite element results show that the yielding is initiated at 110 psig in the inside hoop bars at approximately one-third of the cylinder height (Fig. 15). The outside hoop bars yield soon after the inside hoop bars have yielded. Subsequently, yielding of the diagonal seismic bars and the liner plate in this region takes place at 125 psig and 128 psig, respectively. The liner, which is subjected to initial compressive strains due to the thermal loading, is the last steel member to yield even though it has a lower yield stress. Stresses in the reinforcing bars and liner do not change appreciably after yielding until the onset of strain hardening at about 138 psig. Consequently, additional forces, which arise when the pressure is raised from 128 to 138 psig, are taken by shear stresses and are transferred to the base and dome where the stresses are comparatively lower. This transfer of stresses results in a significant meridional bending action. Strain hardening above 138 psig increases the stresses in hoop bars over the middle third of the cylinder. These stresses reach approximately 94 ksi in inside and outside hoop bars at an internal pressure of 170 psig. At this pressure, normal displacements of the cylindrical wall become very large (exceeding 20"). The finite element analysis above 170 psig was not carried out in Ref. 2, but it was shown by approximate calculations that the hoop and seismic bars would reach their ultimate strength (106 ksi) at 200 psig.

3.3.3 Comparison of Results (Indian Point Containment)

Analytical results discussed above show that the BNL, LASL and MIT finite element models yield varying failure responses for the Indian point containment. A major difference is that the MIT model predicts a hoop stress failure of the containment cylinder at the cylinder mid-height, whereas the BNL and LASL models predict progressive shear failure at the basemat-cylinder intersection. It should be noted, however, that the simplified MIT Model uses many idealizations that would tend to mask a shear type failure through the wall thickness. These idealizations include: (1) only one layer of 4-noded quadrilateral elements is used in the containment wall to model the concrete, (2) the rebars are lumped on the inside and outside faces of the containment wall, and (3) the basemat is not modeled and the containment wall is assumed to be fixed at the base. The errors due to these assumptions on the modeling of shear deformations have been discussed earlier in Section 2.5. In addition, a linear orthotropic model is used in the MIT analysis for modeling the plain concrete. This model would overestimate the concrete strength under high compressive stresses that occur in the outside region of the basemat-cylinder intersection. The cumulative effect of the above approximations is that no shear failure is predicted at the intersection even when the analysis is carried up to 170 psig internal pressure.

While the overall structural responses predicted by the BNL and LASL models are similar, there are, however, two important differences in the two analyses with regards to the shear failure at the basemat-cylinder intersection. The first is that a significant compressive crushing of the concrete is predicted in the LASL analysis at the intersection above 110 psig internal pressure. It is the combined effect of cracking and crushing in the LASL analysis that causes the shear capacity of the concrete to be reduced considerably. In the BNL analysis, however, only large compressive plastic deformation (but no crushing) is predicted in this region of the intersection. In fact, the BNL analysis shows, that the resulting redistribution of stresses prevents compressive crushing of the concrete and the corresponding loss of the shear strength. Based on previous studies[10,11] it is expected that the

plasticity analysis would yield better results for large plastic deformations of concrete under high compressive stresses. The formulations and relative merits of various concrete models have been discussed previously in Section 2.1.

The second difference between the BNL and LASL analyses pertains to the modeling of cracked concrete. As mentioned earlier, in the BNL analysis, the shear stiffness factor for the cracked concrete is reduced as a function of the crack width (Eq. 2-20). It is assumed to be a constant, equal to 0.5, in the LASL model irrespective of single or multiple cracks. It has been shown in several studies[11,14,24] for simple reinforced concrete members, that their shear capacity is over-estimated by a significant amount (for example, by 25% for a reinforced concrete beam), when a large (> 0.2) value of the shear retention factor is utilized. This fact was indeed recognized as a computer code limitation in the LASL evaluation[7]. Thus, it seems that the higher predicted shear capacity of the cracked concrete apparently compensates to some extent for the loss of shear capacity of the compression-crushed concrete. This is probably the reason that the final failure pressure obtained in the LASL analysis (118 psig) is fairly close to that predicted by the BNL model (125 psig).

3.4 Zion Containment Building

The Zion containment building, shown in Fig. 16, is a lightly reinforced, prestressed (post-tensioned) concrete structure. The structure consists of three major parts, namely, a 9 ft. thick basemat, a 3.5 ft. thick cylinder, and a 2.67 ft. thick dome. The inner surfaces of these parts are lined with a 1/4 in. thick ductile steel liner plate. Other basic dimensions and features of the containment are depicted in the figure. A transition ring is provided between the cylinder and the dome which is used to anchor all prestressing tendons of the dome. Tendons for vertical prestressing of the cylinder are anchored on one end to this ring and on the other end to the basemat. Hoop tendons in the cylinder are anchored to six equally-spaced vertical buttresses (not shown) around the cylinder.

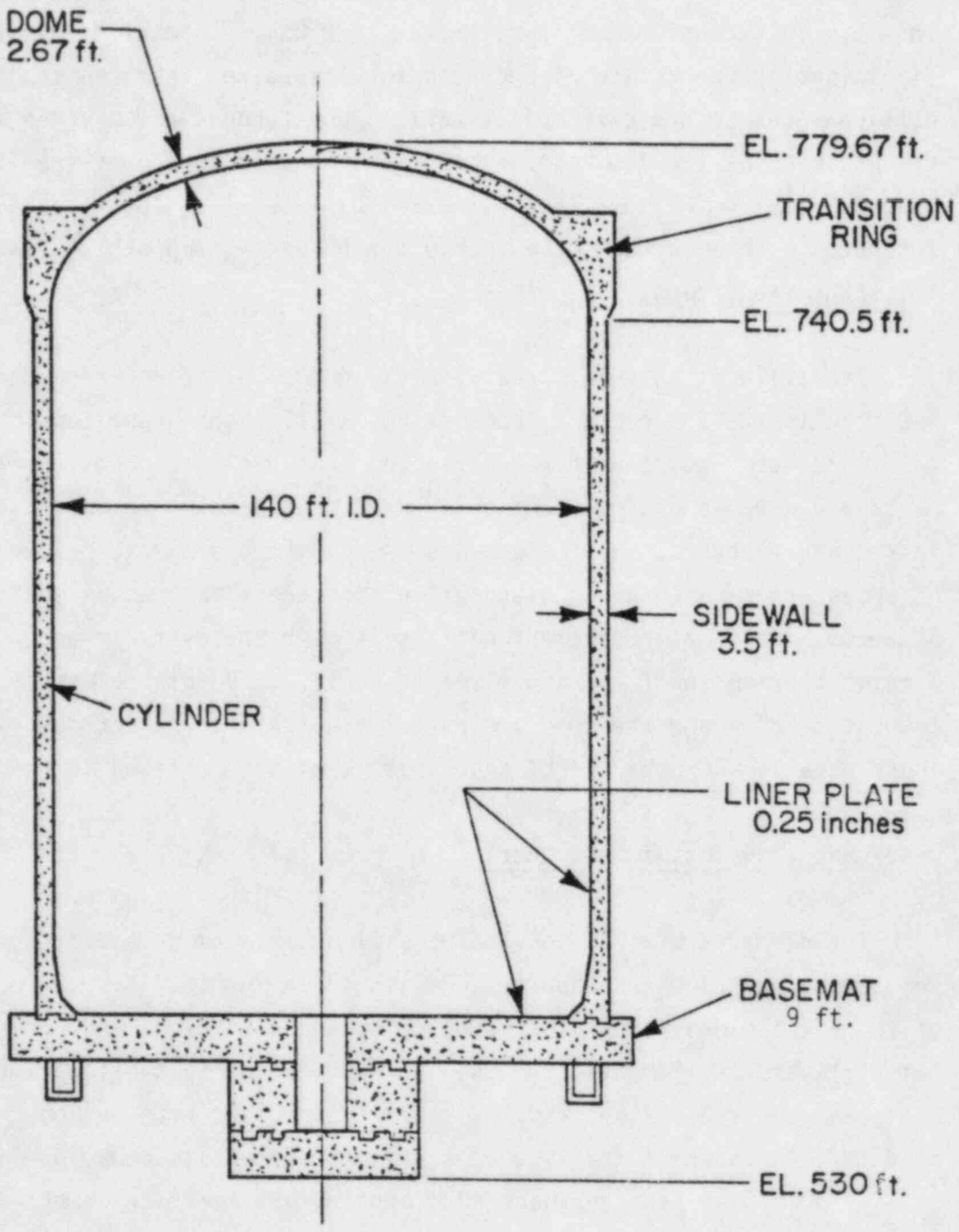

Figure 16. Zion Containment Building

Details of the tendons and rebars in the cylindrical wall are shown in Fig. 17. All tendons consist of ninety 0.25 in diameter steel wires and are initally post-tensioned to aproximately 240 ksi. A total of 216 vertical (meridional) tendons are placed with equal spacings near the inside and outside faces of the cylindrical wall. Hoop tendons are divided into three groups, each having 193 tendons that are anchored to two of the six buttresses spanning 120°. The dome is prestressed by a total of 189 tendons. These are arranged in three groups of 63 tendons with each group at 120° with respect to the other two groups.

The cylinder is reinforced with two groups of reinforcing bars placed near the inside and outside faces of the wall. Each group consists of vertical and hoop rebars with varying sizes and spacings. Heavier reinforcements are used at the cylinder base where high bending moments and shear forces are expected. Unlike the Indian point containment, however, there is no secondary meridional or diagonal reinforcement to provide additional shear strength. Major reinforcement details in both the cylinder and the dome of Zion containment building are given in Table 3. Reinforcement patterns in the transition ring and the dome are rather complex and are not described here. These details and other pertinent information can be found in Ref. [25].

3.4.1 BNL Zion Containment Model

The BNL axisymmetric model of the Zion Containment building, also developed using the NFAP computer code, is shown in Fig. 18. The model consists of 268 eight-noded isoparametric elements and a total of 954 nodes. Six different layers of elements were used through the containment wall thickness to represent the steel liner and the concrete sections with various rebars and tendons. As shown in the figure, a refined element grid was used at the base mat-cylinder intersection where high bending and shear deformations are expected. Element thickness in the grid were carefully selected to closely model the rebar and tendon locations. All rebars and tendons, except the meridional tendons in the cylindrical wall, were modeled within the concrete elements by the smeared composite material approach. Truss elements were used for the meridional tendons in the cylinder in order to model their locations

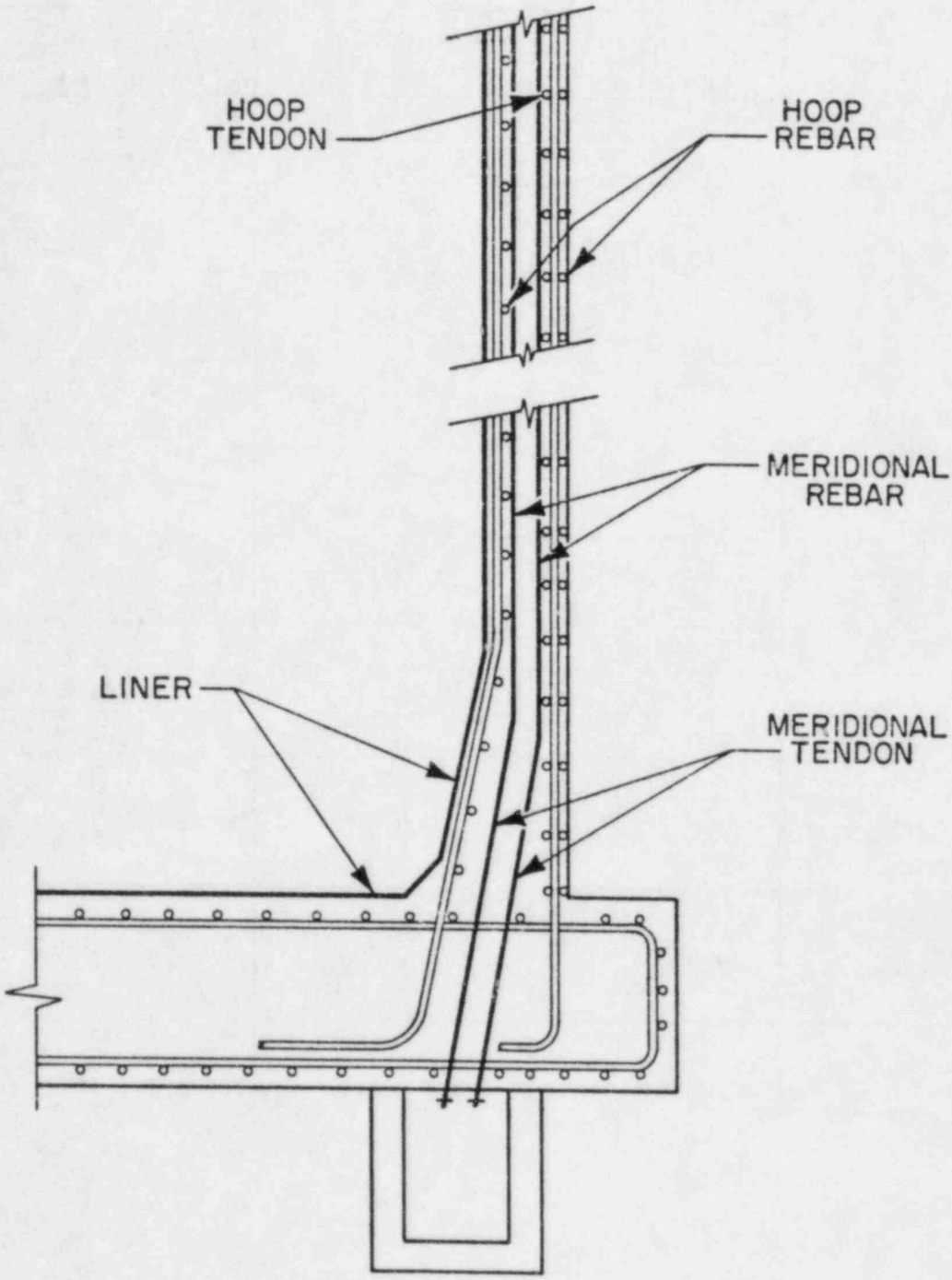

Figure 17. Reinforcements and Tendons in the Zion Containment Cylinder

Table 3. Reinforcement Details of the Zion Containment Cylinder and Dome.

Elevation	Hoop (Inside Face)	Hoop (Outside Face)	Meridional (Inside Face)	Meridional (Outside Face)
565' ~ 565.5'	#10 @ 12"	2 - #11 @ 7"	#18 @ 18"	#18 @ 12" #11 @ 24"
566.5' ~ 570'	#10 @ 12"	2 - #11 @ 7"	#18 @ 18"	#18 @ 12" #11 @ 24"
570' ~ 576.5	#10 @ 12"	#11 @ 7"	#18 @ 18"	#18 @ 12" #11 @ 24"
576.5' ~ 585'	#10 @ 18"	#10 @ 12"	#10 @ 18" #18 @ 18"	#18 @ 12" #10 @ 12"
585' ~ 595'	#10 @ 18"	#10 @ 12"	#10 @ 18" #18 @ 18"	#10 @ 12"
595' ~ 719.5'	None	#10 @ 12"	2 - #10 @ 9"	#10 @ 12" #11 @ 12"
719.5' ~ 729'	#10 @ 12"	#11 @ 10.5"	2 - #10 @ 9"	2 - #11 @ 6"
729' ~ 734.5'	#10 @ 12"	#11 @ 10.5"	2 - #10 @ 9"	2 - #11 @ 6"
734.5' ~ 739.5'	#10 @ 12"	#11 @ 10.5"	2 - #10 @ 9"	2 - #11 @ 6"
739.5' ~ 753'	#10 @ 12"	#10 @ 12"	#10 @ 7"	#11 @ 6" #10 @ 12" #9 @ 12"
753' ~ 758.5'	#10 @ 12"	2 - #10 @ 12"	#10 @ 7"	#11 @ 6" #10 @ 12" #9 @ 12"
758.5 ~ Top	#10 @ 12"	#10 @ 12"	#10 @ 7"	#11 @ 8.2" #10 @ 12"

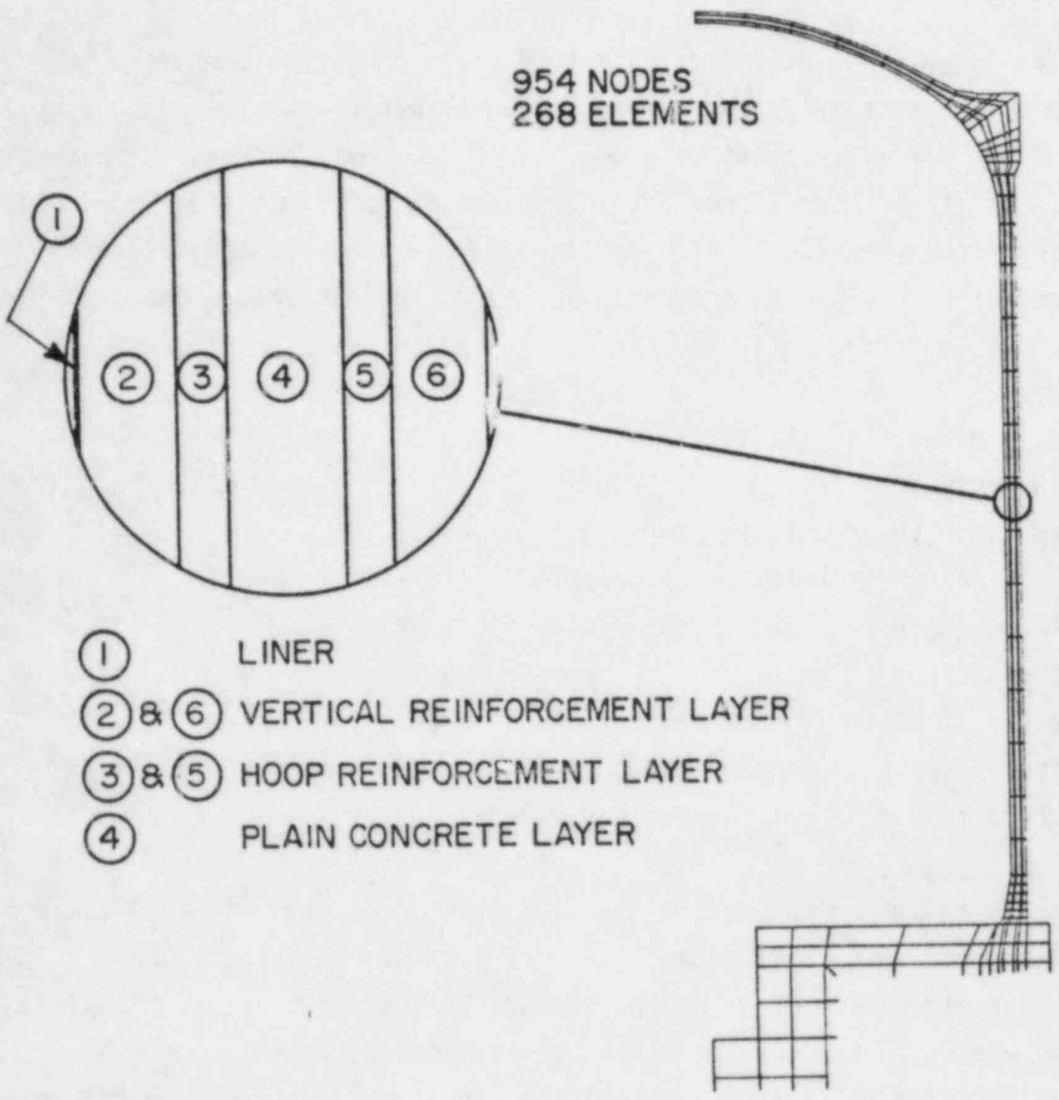

Figure 18. BNL Zion Containment Model

near the basemat-cylinder intersection more accurately. Another set of truss elements were used under the basemat to represent the boundary conditions due to ground restraint. These elements were assigned high spring modulus in compression for the soil stiffness, and zero spring modulus in tension to allow for a possible uplifting of the basemat.

Inelastic material responses of the concrete and steel members were described by, respectively, the Chen and Chen[9] elastic-plastic-fracture model, and the von Mises plasticity model with isotropic hardening. Material parameters for these models were estimated from as-built material properties whenever available, or from their specified design values. The following values were used in the Chen and Chen model for the concrete of the containment cylinder and dome:

Initial Modulus of elasticity = 5,700 ksi
Poisson's ratio = 0.19
Yield strength in uniaxial tension = 0.3 ksi
Yield strength is uniaxial compression = 4.0 ksi
Yield strength in biaxial compression = 5.0 ksi
Fracture strenyth in uniaxial tension = 0.4 ksi
Fracture strength in uniaxial compression = 6.6 ksi
Fracture strain in tension = 0.000125
Fracture strain in compression = 0.003

For the concrete in the basemat, an initial elastic modulus of 5,000 ksi and a fracture strength in uniaxial compression of 5.9 ksi were used. Other material parameters were taken to be the same as specified above. Tension stiffening effect in the cracked concrete was modeled by assigning $\alpha = -0.1$ in Eq. (2-14) for element stress calculations. Shear stiffness of the concrete with cracks was calculated by Eq. (2-20) with a value of $c = 0.5$. Uniaxial stress-strain behavior of the steel members, i.e., liner plate, rebars and tendons, was approximated by simple bi-linear curves with elastic and plastic moduli of 29,000 ksi and 100 ksi, respectively. Yield strength values were taken to be 48.4 ksi for the liner, 67.2 ksi for the rebars, and 222.5 ksi for the tendons. A Poisson's ratio of 0.3 was used for all steel members.

Post-tensioned prestress in the tendons was assumed to be 145 ksi which is roughly 60% of their yield strength. This value represents a loss of 47 ksi from the initial prestress of 192 ksi due to combined effects of creep, shrinkage and stress relaxation. The assumed prestress is taken to be approximately the same as that used in Ref. 7 in order to carry out a comparative evaluation of the analysis results.

3.5 BNL Analysis Results for the Zion Containment

Analysis results for the Zion Containment were obtained for a combined loading of dead-weight, tendon prestress and internal pressure. The entire dead-weight and tendon prestress loads were applied at the beginning of the stepwise nonlinear solution procedure. The internal pressure was applied incrementally with an initial load step of 50 psig. This was subsequently followed by four steps of 5 psig each, raising the internal pressure to 70 psig at which the concrete began to crack in tension. After the crack initiation the step size was reduced to 1 psig. Equilibrium iterations with stiffness updates (i.e., Newton-Raphson procedure) were used for each load step in the nonlinear range. Geometric nonlinear effects were included in the analysis for both the stiffness matrix and load vector calculations.

3.5.1 Deformation Response

The overall deformation response of the Zion Containment is illustrated in Fig. 19 which depicts both the undeformed and deformed (before failure) model shapes. Displacements for the deformed shape are magnified by a factor of 50 for ease of visualization. The figure shows qualitatively an uplifting of the basemat below the cylindrical wall, and high bending deformations near the dome transition ring and the basemat-cylinder intersection. Radial displacements are maximum and nearly uniform in the middle two-thirds of the cylinder. At the top and bottom of the cylinder, the outward displacement growth is restrained by high radial stiffness of the basemat and the dome transition ring.

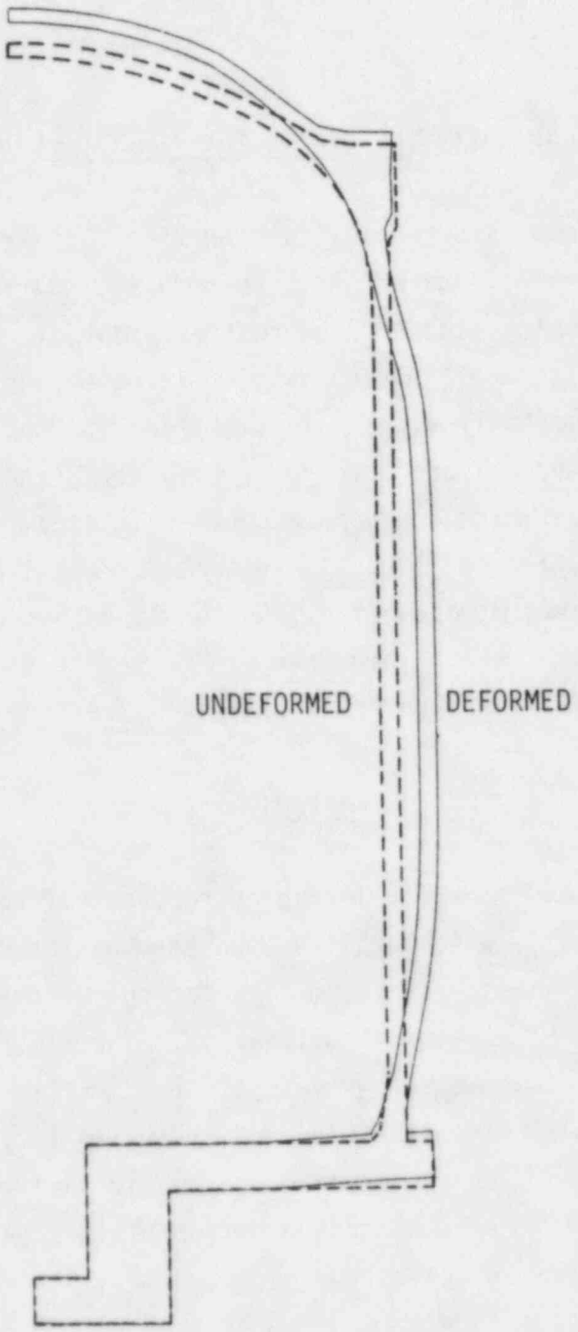

Figure 19. Undeformed and Deformed Shapes of the Zion Containment

Figure 20 shows plots of radial displacement at the cylinder mid-height and vertical displacement at the dome apex versus internal pressure. Initial values of these displacements at zero internal pressure are negative because of the tendon prestress and gravity loadings. The displacement growths from 0 to 85 psig internal pressure are almost linear. Although minor concrete cracks are initiated at 70 psig at the inside surface of the dome transition ring, they do not have any appreciable effect on the two displacements shown in the figure. The displacement curves show rapid nonlinear growth after approximately 85-88 psig internal pressure when the cracks due to meridional and hoop stresses develop, respectively, at the basemat-cylinder intersection and at the cylinder mid-height. The radial displacement increases rather sharply even though a tension-stiffening factor of -0.1 was used in the analysis. This growth rate is, however, reduced after 102 psig when hoop stresses in the cracked concrete are completely released.

3.5.2 Cracking and Shear Failure of Prestressed Concrete

Because of the initial compressive stresses in the prestressed concrete, tension cracks in the Zion Containment are initiated at a considerably higher internal pressure than those in the Indian Point Containment. As mentioned above, initial cracks due to meridional stresses are predicted at 70 psig internal pressure on the inside surface of dome transition ring. These cracks spread slowly in both meridional directions, up the dome and down the cylinder, with increasing pressure. However, because of the thickness of the ring section and the reinforcement in this region, the cracks do not propagate appreciably through the thickness and, consequently, their effect on the overall structural behavior is not significant. Similarly, tension cracks are initiated at 75 psig on the underside of the basemat due to bending stresses associated with the basemat uplift. These cracks also do not penetrate through the thickness and apparently have no significant adverse effect.

Another set of concrete cracks, which eventually results in the containment failure, is initiated at 84 psig internal pressure near the basemat-cylinder intersection. The cracks first appear on the inside surface of the

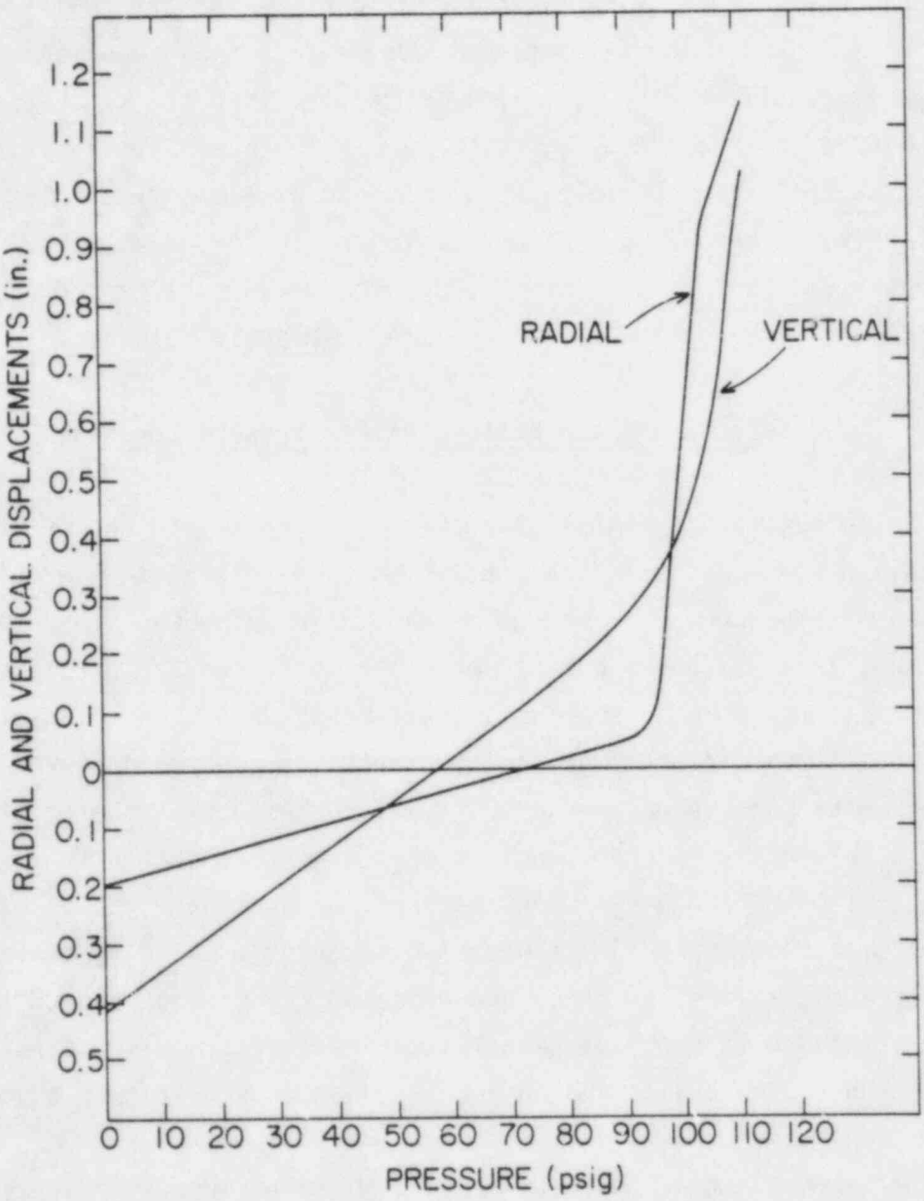

Figure 20. Radial Displacement at Cylinder Mid-Height and Vertical Displacement at Dome Apex Versus Internal Pressure (Zion Containment)

cylinder, one element thickness (Fig. 18) above the intersection. These cracks are initially formed in a horizontal plane (perpendicular to the meridional direction) by the high tensile meridional stresses. With increasing internal pressure, the cracks propagate both vertically and radially through the wall thickness. The cracks in the interior of the wall are formed at various angles from the horizontal plane along the principal stress directions controlled by both the meridional and shear stresses. At 95 psig, these cracks penetrate through 25% of the wall thickness at the intersection. Crack penetration through 36%, 64% and 76% of the wall thickness occurs at 101, 105 and 111 psig internal pressure, respectively. Furthermore, secondary cracks caused by the tensile component of the high shear stresses at the intersection are initiated at 105 psig. When this occurs, the concrete fails in shear losing substantially its capacity to resist the shear forces. The secondary cracks also spread through the wall thickness with increasing pressure, thus propagating the shear failure of the concrete. The numerical solution gives divergent results above 111 psig internal pressure because of the extensive shear failure. This value is, therefore, predicted to be the failure pressure of the Zion Containment. As mentioned previously in the discussion pertaining to the Indian Point evaluations, the numerical divergence of the solution is not caused by large displacements but is due to actual shear failure. That is, the elements in the intersection region have suffered multiple cracking and thus cannot absorb any further shear forces.

The containment cylindrical wall also cracks in the vertical plane due to the hoop stresses. These cracks first appear at the cylinder mid-height when the internal pressure reaches 87 psig. The cracks spread quickly covering the middle two-thirds of the cylinder at 102 psig. Because of the radial restraints from the basemat and the dome transition ring, vertical cracks are not formed in these two sections of the cylinder. Consequently, the cracked region remains essentially the same up to 111 psig at which the shear failure occurs at the cylinder base. Additional cracking is, however, found to occur near the dome apex at 109 psig due to both hoop and meridional stresses. These cracks remain confined to the apex region up to the failure pressure, 111 psig.

Bending deformations at the basemat-cylinder intersection give rise to high meridional compressive stresses in the outside region of the cylinder base. These stresses result in local plastic deformation of the concrete. The maximum compressive stress in the concrete is -3.5 ksi at 111 psig internal pressure, which is well within the failure envelope for crushing, and thus no crushing of concrete is predicted. This stress condition is similar to that of the Indian Point containment.

3.5.3 Stresses in the Steel Members

Because of the instantaneous elastic deformations under post-tensioning and gravity loads, the liner and rebars of the containment wall are subjected to initial compressive stresses. Tendon prestresses are reduced correspondingly from 145 ksi to approximately 143 ksi. The stresses in all steel members increase (algebraically) with rising internal presssure, except in the outside meridional rebar near the basemat-cylinder intersection where they decrease. These stresses, however, do not exceed the yield strength of any member even at the failure pressure of 111 psig.

Analysis results show that the liner would be the first steel member to yield if there were no shear failure at the cylinder base and the internal pressure could be raised further. As expected, hoop stresses in the liner is highest at the cylinder mid-height, and the meridional stress is highest at the basemat-cylinder intersection. Figure 21 depicts plots of these two stresses versus internal pressure. Initial hoop and meridional liner stresses are -8.4 ksi and -9.6 ksi, respectively. They increase linearly at moderate rates up to an internal pressure of approximately 85-87 psig when cracking of the concrete is initiated in the two regions. The stresses then increase rapidly because of the loss of concrete stiffness and the transfer of forces from the cracked concrete to the steel members. The hoop stress increases more sharply since the entire middle two-third of the cylinder is cracked within the pressure range 87-102 psig. This stress reaches 32 ksi at 102 psig internal pressure. Above this pressure the rate of the growth of hoop stress is decreased to some extent because there is no additional transfer of concrete stresses to the steel members which are still elastic. The liner hoop

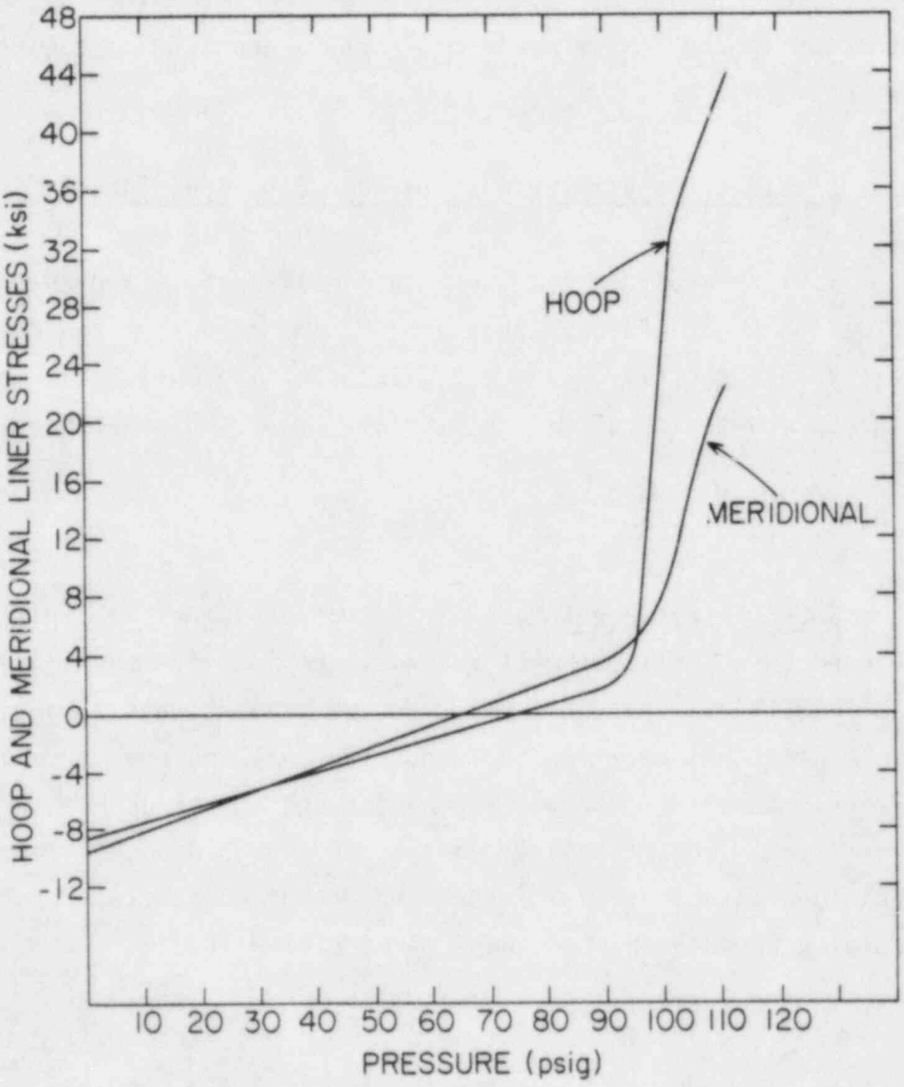

Figure 21. Liner Hoop Stress at Cylinder Mid-Height and Meridional Stress at Basemat-Cylinder Intersection (Zion Containment)

stress reaches 44 ksi at the final failure pressure of 111 psig. The increase of meridional stress in the liner is more gradual as shown in the figure. Maximum value of this stress is only 22.4 ksi at 111 psig internal pressure.

Hoop and meridional stresses in the rebars and tendons have very similar growth patterns. Maximum hoop stresses in the hoop rebars and tendons at cylinder mid-height reach 38.1 ksi and 183.5 ksi, respectively, prior to the containmenat failure at 111 psig. The corresponding values for meridional stresses in the inside meridional rebars and tendons are, respectively, 20.2 ksi and 180.0 ksi.

3.6 Previous Analysis Results for the Zion Containment

Failure analyses for the Zion containment were previously carried out by Sargent & Lundy (S&L) Engineers[17,26], and by Butler and Fugelso[7] at the Los Alamos Scientific Laboratory (LASL). The analytical models used in these studies and the predicted results are briefly discussed below.

3.6.1 S&L and LASL Containment Models

S&L Finite Element Model - In this axisymmetric finite element model, layered thin shell elements were used to idealize the containment geometry (see Fig. 22). The model employed 140 elements and 78 nodes to represent the containment, as well as the foundation soil and the tendons. The thin shell elements used six concrete layers through the thickness and additional two to five layers for the inside and outside rebars and the liner. The layering technique was utilized to trace the extent of concrete cracking and rebar yielding through the thickness of each element.

Hoop tendons in the cylinder were represented by additional elements connecting the nodes of the corresponding concrete elements. The vertical tendons were modeled by two elements with nodes at the top and bottom of the cylinder. The dome tendons were modeled similarly using the nodes of the concrete elements along the dome meridian. Prestressing tendon stresses were induced by an externally applied pressure on the cylinder and dome, and by concentrated loads at the top and bottom anchorages of the cylinder.

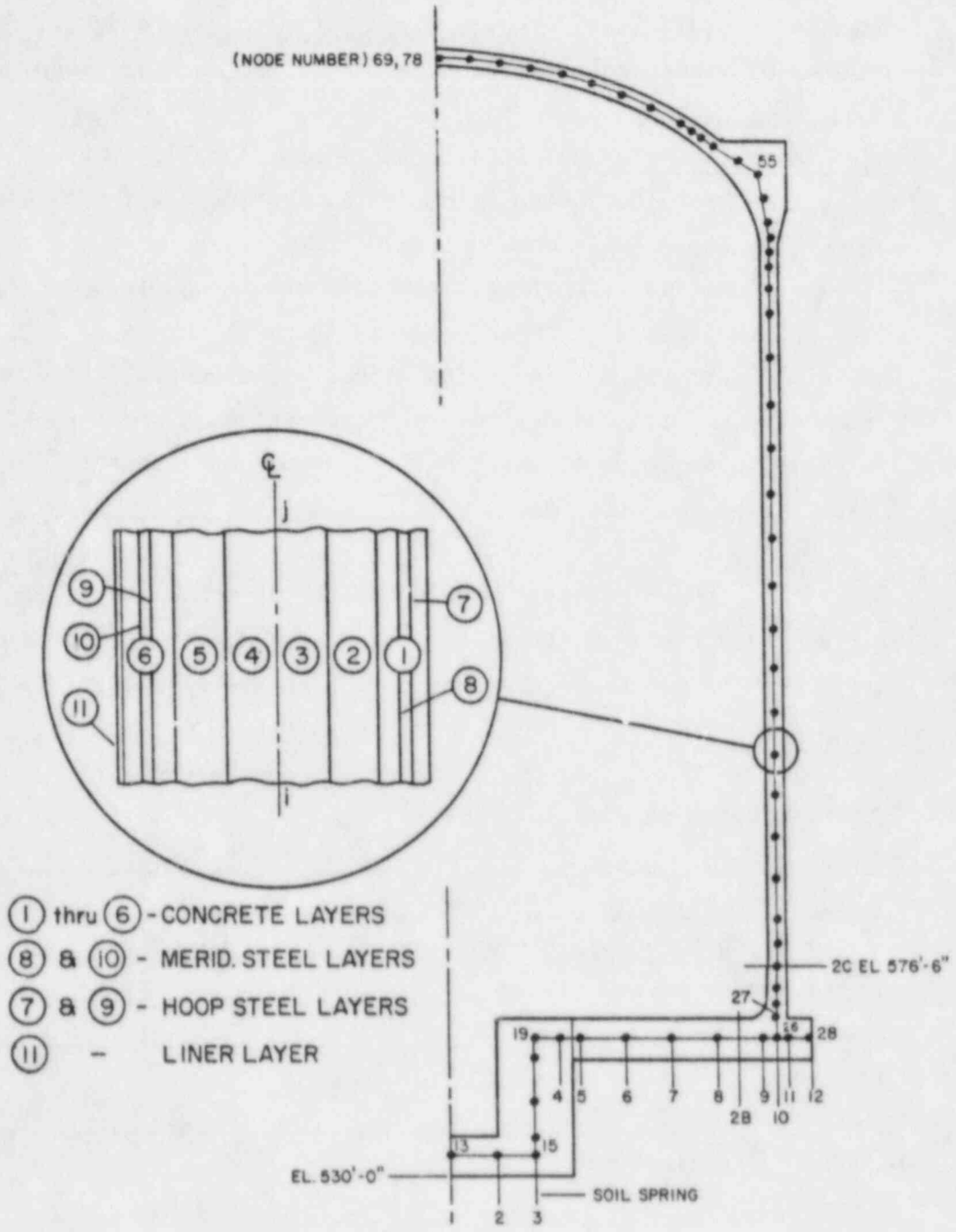

Figure 22. S&L Zion Containment Model (Ref. 26)

Material properties for the concrete and steel members, although not given specifically, were apparently taken to be the same as those employed in a companion analysis using approximate hand calculations.[26] In these calculations, tensile strength of the concrete in the cylinder and dome was assumed to be 0.467 ksi. Average yield strength values of 222.5 ksi for the tendons, 67.2 ksi for the rebars, and 48.4 ksi for the liner, were used.

LASL Finite Element Model - This containment model is very similar to that used by LASL for the Indian Point containment, and was also developed for analysis by the ADINA computer code.[6] Four layers of two dimensional axisymmetric elements were utilized to model the containment cylinder and dome, and two layers of these elements to model the basemat (see Fig. 23). The steel liner was modeled by thin membrane elements. Ring and truss elements were used to model the reinforcement bars and tendons. In addition, nonlinear spring elements were employed under the basemat to simulate one-way (compressive) soil stiffness.

The nonlinear material models for the concrete and steel members were the same as those used for the Indian Point containment (see Section 3.3.1). The following material properties were used for the concrete:

	Basemat	Above Basemat
Tangent modulus of elasticity at zero strain	5,000 ksi	5,700 ksi
Poisson's ratio	0.19	0.19
Uniaxial cutoff tensile stress	0.4 ksi	0.4 ksi
Uniaxial maximum compressive stress	5.9 ksi	6.6 ksi
Corresponding uniaxial compressive strain	0.002	0.002
Uniaxial ultimate compressive stress	4.3 ksi	4.9 ksi
Corresponding ultimate compressive strain	0.003	0.003

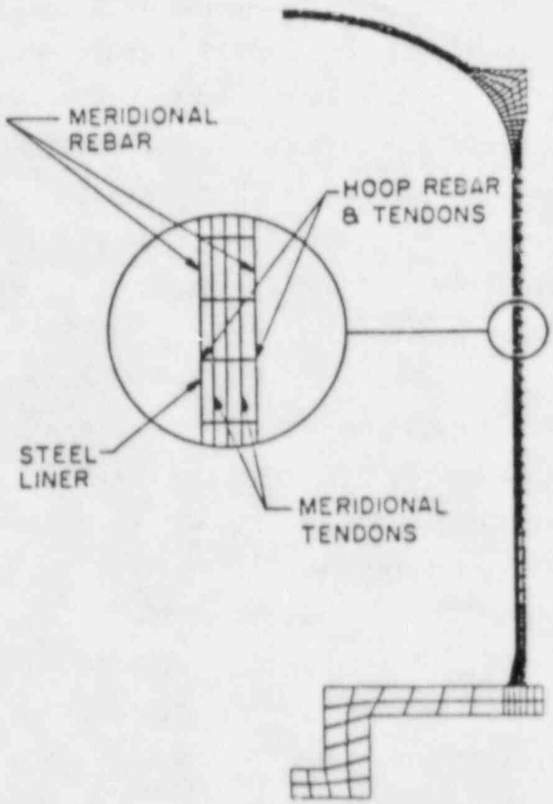

Figure 23. LASL Zion Containment Model (Ref. 7)

Uniaxial stress-strain behavior of the steel members was idealized by elastic-plastic bilinear curves. As-built mean yield strength values of 222.5 ksi, 67.2 ksi and 48.4 ksi were used for the tendons, the rebars and the liner, respectively. Elastic and plastic tangent moduli of 29,000 ksi and 0.29 ksi, respectively, were assumed for all steel members.

3.6.2 S&L and LASL Analysis Results (Zion Containment)

S&L Analysis Results - Based on the results obtained from the axisymmetric thin shell finite element model, S&L predicts that hoop stresses in the central cylindrical region are the most critical stresses. The results show that through-thickness concrete cracks due to hoop stresses develop at 70.5 psig internal pressure. Tendon hoop stresses increase sharply following the cracking of concrete (Fig. 24). With further increase in pressure, the tendon stresses grow almost linearly reaching the average yield strength (222.5 ksi) at 134.4 psig. These values were found to compare very well with the approximate hand calculations also presented in the report.[26]

No details were given in the report for the concrete stresse in the basemat-cylinder intersection region. Potential shear failure of the concrete in this region was, therefore, not evaluated directly from the finite element analysis. Rather, margins of safety were determined for various sections of the containment based on ASME BPV-III-2, "Code for Concrete Reactor Vessels and Containments", (Ref. 27). At the internal pressure of 134.4 psig, the minimum margin of safety for radial shear was found to be 1.15 at a basemat section 2B (Fig. 22) close to the cylindrical wall. The corresponding margins of safety at a cylindrical section 2C (Fig. 22) above the basemat-cylindrical intersection was calculated to be 1.16. Pertinent normal and shear stresses for these calculations were obtained from another finite element model (no details given) that was carried out when the containment was initially designed.

The internal pressure capacity of the containment was thus estimated to be 134 psig corresponding to the yielding of hoop tendons in the middle cylindrical region.

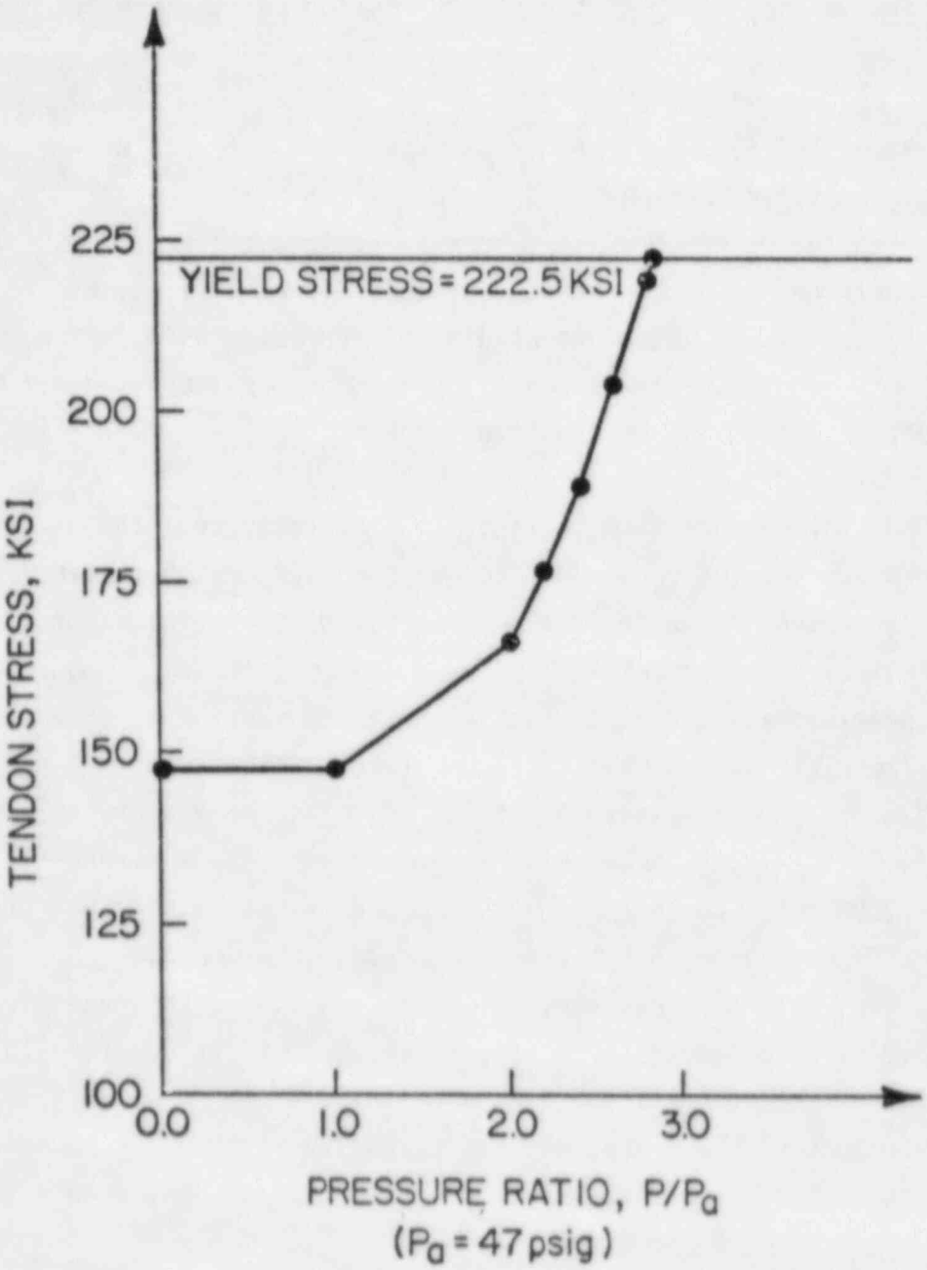

Figure 24. Tendon Hoop Stress at Cylinder Mid-Height - S&L Analysis for the Zion Containment (Ref. 26)

LASL Analysis Results - Analysis results indicate that considerable cracking occurs at 85 psig internal pressure on the inside of the cylindrical wall at its intersection with the basemat, and on the inside of the dome transition ring. The mid-section of the cylindrical sidewall undergoes cracking perpendicular to the hoop direction at 95 psig. In addition, dome cracking perpendicular to the hoop direction takes place between 100 and 105 psig.

Steel reinforcement and tendons yield at the apex of the dome resulting in large displacements in this region at 125 psig internal pressure (Fig. 25). According to the LASL report[7], it was realized that the model used did not adequately represent the actual stiffness in this (i.e., the apex) region. Therefore, when an increment of 0.5 psi above 125 psig internal pressure was applied to the containment model, convergent results could not be obtained because of very large deformations.

LASL also reports that significant concrete cracking at the basemat cylinder intersection occurs due to the combined action of tensile bending and shear stresses. With increasing internal pressure, additional cracking occurs perpendicular to the initial cracks. The concrete then should lose most of its shear-carrying capacity. LASL, however, notes that because of computer code limitations, its analytical model still retains 50% of the original shear stiffness. LASL assesses the effect of retaining higher shear stiffness as follows: "To insure that this phenomenon does not mask a failure below 125 psig (0.86 Mpa), we checked the structure by determining whether the steel in this area could absorb the shear carried in the concrete. At 125 psig (0.86-Mpa) internal pressure, the steel can absorb this additional shear without yielding". In spite of this assessment, LASL writes in the conclusion section of the report that, "the apparent failure mode for the Zion containment is loss of overall structural integrity in the high shear and moment regions as the base of the cylindrical sidewall. This occurs at 125 psig (0.86 Mpa) internal pressure".

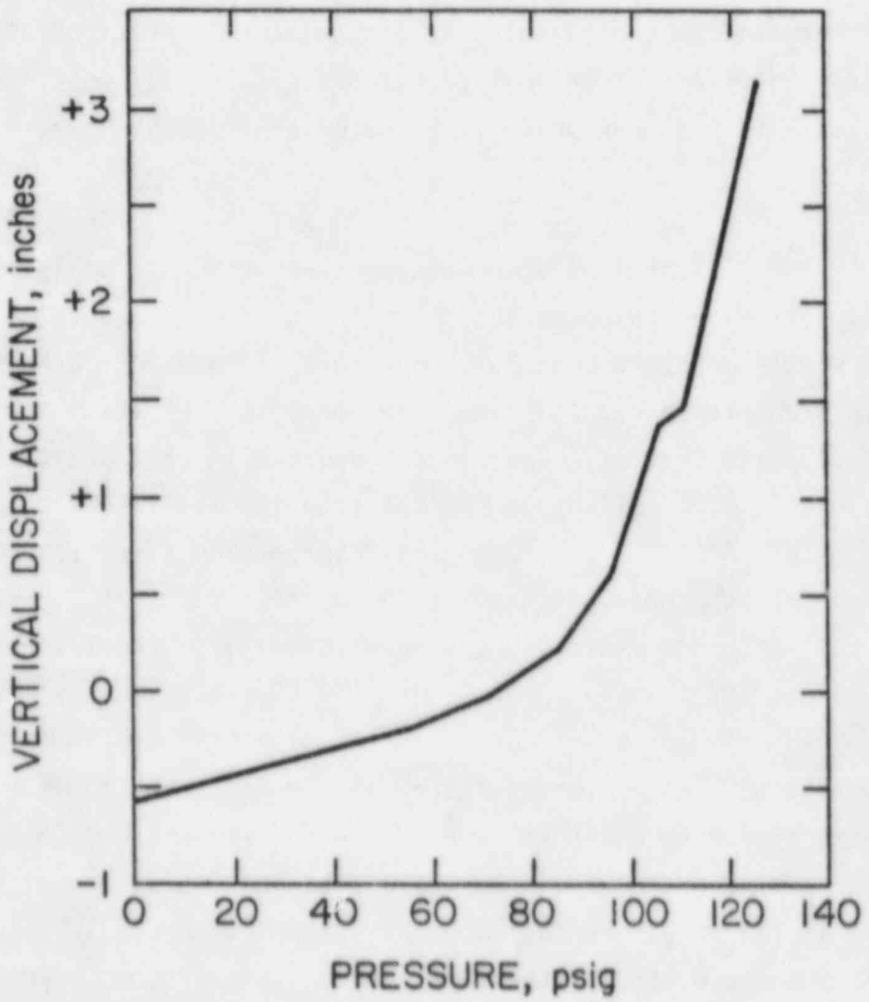

Figure 25. Vertical Displacement at the Dome Apex - LASL Analysis for the Zion Containment (Ref. 7)

Because of the ambiguity about the shear failure mode at 125 psig, LASL also goes on to predict a second failure mode which involves yielding of the hoop rebars and tendons in the cylindrical wall. This failure mode is estimated to occur at 136.4 psig internal pressure.

3.6.3 Comparison of Results (Zion Containment)

As discussed previously, BNL analysis results for the Zion containment predict shear failure due to multiple concrete cracks that occur at the basemat-cylinder intersection at an internal pressure of 111 psig. This failure is not associated with any prior large deformation or yielding of the steel members.

The BNL results obviously do not agree with the S&L analysis in which the failure is determined to be caused by yielding of the hoop tendons at 134 psig. It should be noted that layered thin shell elements are used by S&L for the analysis and these cannot adequately model the complex interactions between out-of-plane (radial) shear forces and bending moments (see Section 2.5.3). This is especially true for the intersection region where multiple cracks develop. Although S&L found the intersection to satisfy ASME code criteria for radial shear, it needs to be pointed out that the stress values used for the ASME code evaluations were obtained from the inadequate thin shell model results.

As mentioned, LASL determined two failure pressures for the containment. One of these is due to shear failure at the containment base which is inferred to occur at 125 psig, and the other is due to steel yielding at the cylinder mid-height at 136 psig. Furthermore, at 125 psig, the analysis predicts large deformations and yielding of the steel members at the dome apex. According to LASL, this caused numerical instability above 125 psig and thus, the analysis could not be continued with higher pressures. This yielding was not obtained either by BNL or by S&L and, in fact, LASL indicates that its model did not

adequately represent the stiffness in the apex region. Thus, the shear failure at 125 psig was not directly obtained from the computer analysis. In fact, it is not clear how LASL deduces a shear failure at 125 psig, especially since it maintains that its code limitations (pertaining to shear in multiply cracked concrete) does not mask the shear failure up to 125 psig because the steel can absorb the concrete shear without yielding.

4. SUMMARY AND CONCLUSIONS

An intensive independent review of failure analysis of reinforced and prestressed concrete containments subjected to accidental internal pressures was performed. The material models used for describing the linear and nonlinear behavior of concrete and steel were reviewed in depth. Special attention was focused on post-cracking behavior of concrete which controls one of the containment failure modes, i.e., the shear failure. Various finite elements idealizations utilized for containment analysis were reviewed. The effects of major assumptions pertaining to: (1) containment geometry, (2) basemat restraint, (3) finite element mesh, (4) rebar locations, and (5) rebar orientations were assessed. Finally, failure analyses of two selected containments were independently performed and results were compared with those presented in the literature.

Briefly stated, the major conclusions and findings are as follows:

(a) The failure of concrete containments under severe internal pressure occurs either due to shear failure of the concrete at the basemat-cylinder intersection or from extensive hoop yielding of the steel in the central cylindrical section of the containment.

(b) The analytical predictions for failure due to hoop yielding of the steels are relatively insensitive to various assumptions and idealizations with respect to both material and geometric models. In fact, this failure mechanism can be estimated within a reasonable range of accuracy even with simple hand calculations.

(c) The shear failure mode however cannot be predicted by simple analytical models. This failure mode is highly dependent on accurate modeling of the concrete, especially for post cracking behavior and for high compressive plastic deformation. This failure mechanism also requires refined finite element meshes that can properly describe the deformation field in regions subjected to high bending and shear forces.

(d) Since bending and shear deformations are inter-related, the shear failure is influenced by the locations of the meridional rebars (and tendons). Simple models in which the steel members are lumped on the inside and outside faces of the containment wall, overestimate the shear capacity of the containment structures.

(e) With respect to the independent analysis, BNL evaluated the failure of the Indian Point and Zion containments under accidental pressures and gravity loadings and determined that both of these would fail due to loss of shear capacity at the basemat-cylinder intersection. The failure pressure for the Indian Point Containment is calculated to be 125 psig, while that of the Zion containment is determined to be 111 psig.

(f) In a previous analysis for the Indian Point containment, MIT predicts failure due to hoop stresses in the cylindrical section. It is estimated that the rebars in this section would reach their ultimate strength at about 200 psig internal pressure. For the same containment, LASL predicts that shear failure at the basemat-cylinder intersection would occur at 118 psig.

(g) Although the values for failure pressure predicted by BNL and LASL for the Indian Point containment are close, the actual stiffness and stress conditions are quite different. LASL results show significant compressive crushing of the concrete in the outer areas of the cylinder-basemat intersection, and a corresponding loss of shear stiffness in the crushed region. BNL results show compressive plastic deformation in this region but no compression crushing or loss of shear stiffness. On the other hand, because of computer code limitations in the LASL analysis, a higher

shear stiffness is retained for multiply cracked concrete in the tensile region of the intersection. These two effects (i.e., the crushing and higher shear stiffness of multiply cracked concrete) apparently compensate each other in this particular case, and thus result in the prediction of 118 psig failure pressure.

(h) For the Zion containment, an analysis performed by S&L determined failure due to hoop steel yielding in the middle cylindrical section at 134 psig. LASL reports two failure pressures, one due to shear failure near the basemat-cylinder intersection at 125 psig, and the second due to hoop steel yielding in the cylinder at 136 psig. As discussed in the text, LASL was not able to continue the analysis above 125 psig because of large deformations and yielding of the steel members at the dome apex which resulted in numerical instabilities. Thus, the shear failure at 125 psig was not directly obtained from the computer analysis. From the review of the LASL report, it is not clear how a shear failure was deduced to occur at 125 psig, especially since it is stated that at this pressure the steel can still absorb the concrete shear without yielding.

(i) Both S&L and MIT used simplified analytical models which, as summarized in items (c) and (d), cannot adequately describe the shear failure. This is the main reason that they predicted failure at higher pressures caused by yielding of hoop steels in the central cylindrical sections. It is BNL's opinion that shear failure takes place at lower pressure as described in (e) above and in the text.

REFERENCES

1. Kupfer, H.B., and Gerstle, K.H., "Behavior of Concrete Under Biaxial Stresses", Journal of the Engineering Mechanics Division, ASCE, 99 (1973), pp. 852-866.

2. Fardis, M.N., Nacar, A. and Delichatsios, M.A., "Reinforced Concrete Containment Safety Under Hydrogen Explosion Loading", Report No. NUREG/CR-2898, U.S. Nuclear Regulatory Commission, Washington, DC, September 1982.

3. Gerstle, K.H., "Simple Formulation of Biaxial Concrete Behavior", Journal of the American Concrete Institute, 78 (1981), pp. 62-68.

4. Darwin, D. and Pecknold, D.A., "Nonlinear Biaxial Stress-strain Law for Concrete", Journal of the Engineering Mechanics Division, ASCE, 103 (1977), pp. 229-241.

5. Bathe, K.J. and Ramaswamy, S., "On-Three-Dimensional Nonlinear Analysis of Concrete Structures", Nuclear Engineering and Design, 52 (1979), pp. 385-409.

6. Bathe, K.J., "ADINA. A Finite Element Program for Automatic Dynamic Incremental Nonlinear Analysis," Report 82448-1, Acoustics and Vibration Laboratory, Department of Mechanical Engineering, Massachusetts Institute of Technology, Cambridge, MA, 1978.

7. Butler, T.A. and Fugelso, L.E., "Response of the Zion and Indian Point Containment Buildings to Severe Accident Pressures," Report prepared for the U.S. Nuclear Regulatory Commission, NUREG/CR-2569, LA-9301-MS, May 1982.

REFERENCES (Cont'd)

8. Jung, J., "Response of Watts Bar, Main Yankee and Bellefonte Containments to Static Internal Pressurization", Proceedings of the ANS/ENS International Meeting on Light Water Reactor Severe Accident Evaluation, Cambridge, MA, August 28 - September 7, 1983.

9. Chen, A.C.T. and Chen, W.F., "Constitutive Relations for Concrete", Journal of the Engineering Mechanics Division, ASCE, 101 (1975), pp. 465-481.

10. Chen, W.F., Suzuki, H. and Chang, T.Y., "End Effects of Pressure Resistant Concrete Shells", Journal of Structural Division, ASCE, 106(1980), pp. 751-771.

11. Taniguchi, H., "Nonlinear Analysis of Reinforced Concrete Structures by Finite Element Method", Ph.D: dissertation, Department of Civil Engineering, University of Akron, Akron, OH, May 1984.

12. Sharma, S., Reich, M. and Chang, T.Y., "Nonlinear Finite Element Analysis of Reinforced Concrete Mark III Containment Under Pressure and Gravity Loads", Transaction of SMiRT 7, Paper No. J 2/8. Chicago, IL, August 1983.

13. Leombruni, P., Buyukozturk, O. and Connor, J.J., "Analysis of Shear Transfer in Reinforced Concrete with Application to Containment Wall Specimens", Report to U.S. Nuclear Regulatory Commission, NUREG/CR-1085, Massachusetts Institute of Technology, Cambridge, MA, 1979.

14. Al-Mahaidi, R.H.S. and Nilson, A.H., "Nonlinear Finite Element Analysis of Reinforced Concrete Deep Members", Report 79-1, Department of Structural Engineering, Cornell University, Ithaca, NY, 1979.

15. Chang, T.Y. and Aoki, H., "A Constitutive Model for Structural Analysis of Fusion Magnets", Nuclear Engineering and Design, 58 (1980), pp. 237-245.

16. Stevenson, M.G. (complied by), "Report of the Zion (Indian Point Study , Volume II", Report No. NUREG/CR-1411, U.S. Nuclear Regulatory Commission, Washington, DC, April 1980.

17. Walser, A., "Primary Containment Ultimate Capacity of Zion Nuclear Power Plant for Internal Pressure Load", Proceedings of the Workshop on Containment Integrity, Vol. II of II, NUREG/CP-0033, U.S. Nuclear Regulatory Commission, Washington, DC, 1982.

18. Dunham R.S., Rashid, Y.R. and Tang, Y.K, "Recent Results on the Evaluation of the Overpressure Response of Concrete and Steel Containments", Proceedings of the Second Workshop on Containment Integrity, NUREG/CP-0056, U.S. Nuclear Regulatory Commission, Washinyton, DC 1984.

19. Dooley, W.T., Macek, R.W. and Sadik, S., "Ultimate Pressure Capacity Analysis of a Post-Tensioned Reinforced Concrete Nuclear Reactor Containment Building", Work supported by U.S. DOE Contract No. DE-AC07-76ID01570 at EG&G, Idaho, Inc., Idaho Falls, Idaho, presented at ASME Pressure Vessel and Piping Conference in Portland, OR, 1983.

20. Final Safety Analysis Report - Indian Point Nuclear Generating Unit No. 3, Consolidated Edison Company of New York, Inc., Vol. II, Docket No. 50286.

21. Prachuktam, S., Reich, M., Gardner, D. and Chang, T.Y., "NFAP - The Nonlinear Finite Element Analysis Program, User's Manual - Version 1977", Report No. BNL-NUREG-24599, Department of Nuclear Energy, Brookhaven National Laboratory, Upton, NY, March 1978.

22. Von Riesemann, W.A., Huerta, M., Chen, E-P. and Swenson, D.V., "Structural Response of the Indian Point 2 and Indian Point 3 Containment Buildings", Section 3.2, Report of the Zion/Indian Point Study: Vol. 1, prepared by W.B. Murfin, Sandia National Laboratory, Albuquerque, NM, Report No. NUREG/CR-1410, SAND80-0617/1, August 1980.

23. Mondkar, D.P. and Powell, G.H., "ANSR-I: General Purpose Program for Analysis of Nonlinear Structural Response", Report No. EERC 75-37, Earthquake Engineering Research Center, University of California, Berkeley, CA, December 1975.

24. Cedolin, L. and Poli, S.D., "Finite Element Studies of Shear Critical Beam", Journal of the Engineering Mechanics Division, Vol. 103, No. EM3, June 1977.

25. Final Safety Analysis Report - Zion Nuclear Generating Unit No. 2, Commonwealth Edison Company, Chicago, IL, Vol. VIII, Docket No. 50304.

26. "Primary Containment Ultimate Capacity of Zion Nuclear Power Plant for Internal Pressure Load", Appendix 4.4.1, a study prepared by Sargent & Lundy Engineers, Chicago, IL for Commonwealth Edison Company, Chicago, IL, November 1980.

27. Code for Concrete Reactor Vessels and Containments, ASME Boiler and Pressure Vessel Code, Section III, Nuclear Power Plant Components, Division 2, 1980.

(7-77) U NUCLEAR REGULATORY COMMISSION

BIBLIOGRAPHIC DATA SHEET

NUREG/CR-4149
BNL-NUREG-51857

4. TITLE AND SUBTITLE *(Add Volume No., if appropriate)*

Ultimate Pressure Capacity of Reinforced and Prestressed Concrete Containments

2. *(Leave blank)*

3. RECIPIENT'S ACCESSION NO.

7. AUTHOR(S)

S. Sharma, Y.K. Wang and M. Reich

5. DATE REPORT COMPLETED

MONTH	YEAR
January	1985

9. PERFORMING ORGANIZATION NAME AND MAILING ADDRESS *(Include Zip Code)*

Brookhaven National Laboratory
Upton, NY 11973

DATE REPORT ISSUED

MONTH	YEAR
May	1985

6. *(Leave blank)*

8. *(Leave blank)*

12. SPONSORING ORGANIZATION NAME AND MAILING ADDRESS *(Include Zip Code)*

Division of Engineering
Office of Nuclear Reactor Regulation
U.S. Nuclear Regulatory Commission
Washington, DC 20555

10. PROJECT/TASK/WORK UNIT NO.

11. CONTRACT NO.

A-3723

13. TYPE OF REPORT

PERIOD COVERED *(Inclusive dates)*

15. SUPPLEMENTARY NOTES

14. *(Leave blank)*

16. ABSTRACT *(200 words or less)*

This report presents the results of an in-depth evaluation of current modeling techniques and analysis procedures for determining ultimate pressure capacity of reinforced and prestressed concrete containments. The material models used for describing the nonlinear material behavior of concrete and steel are reviewed in detail. Special attention is focused on post-cracking behavior of concrete which controls one of the containment failure modes, i.e., the shear failure. Various finite element idealizations utilized for containment analysis are reviewed. The effects of major assumptions pertaining to containment geometry, basemat restraint, finite element mesh, rebar locations and orientations, are evaluated. Finally, failure analyses of two selected reinforced and prestressed concrete containments are performed and results are compared with those presented in the literature.

17. KEY WORDS AND DOCUMENT ANALYSIS

17a. DESCRIPTORS

Reinforced and Prestressed, Concrete Containments, Failure Analysis, Shear Failure, Finite Elements, Nonlinear Models

17b. IDENTIFIERS/OPEN-ENDED TERMS

18. AVAILABILITY STATEMENT

Unlimited

19. SECURITY CLASS *(This report)*
Unclassified

21. NO. OF PAGES

20. SECURITY CLASS *(This page)*
Unclassified

22. PRICE
$

NRC FORM 335 (7-77)

NUREG/CR-4149

ULTIMATE PRESSURE CAPACITY OF REINFORCED AND PRESTRESSED CONCRETE CONTAINMENTS

MAY 1985